The Astrophysical Journal, 890:52 (19pp), 2020 February 10 https://doi.org/10.3847/1538-4357/ab64e9

The Strikingly Metal-rich Halo of the Sombrero Galaxy*

Roger E. Cohen[1], Paul Goudfrooij[1], Matteo Correnti[1], Oleg Y. Gnedin[2], William E. Harris[3], Rupali Chandar[4], Thomas H. Puzia[5], and Rubén Sánchez-Janssen[6]
[1] Space Telescope Science Telescope Institute, 3700 San Martin Drive, Baltimore, MD 21218, USA; rcohen@stsci.edu
[2] Department of Astronomy, University of Michigan, Ann Arbor, MI 48109, USA
[3] Department of Physics & Astronomy, McMaster University, Hamilton, ON L8S 4M1, Canada
[4] Department of Physics & Astronomy, University of Toledo, Toledo, OH 43606, USA
[5] Institute of Astrophysics, Pontificia Universidad Católica de Chile, Avenida Vicuña Mackenna 4860, 7820436 Macul, Santiago, Chile
[6] STFC UK Astronomy Technology Centre, The Royal Observatory Edinburgh, Blackford Hill, Edinburgh, EH9 3HJ, UK
Received 2019 November 11; revised 2019 December 19; accepted 2019 December 20; published 2020 February 12

Abstract

The nature of the Sombrero galaxy (M104 = NGC 4594) has remained elusive despite many observational studies at a variety of wavelengths. Here we present *Hubble Space Telescope* imaging of two fields at ∼16 and 33 kpc along the minor axis to examine stellar metallicity gradients in the extended spheroid. We use this imaging, extending more than 2 mag below the tip of the red giant branch, in combination with artificial star tests to forward model observed color–magnitude diagrams, measuring metallicity distribution functions (MDFs) at different radii along the minor axis. An important and unexpected result is that the halo of the Sombrero is strikingly metal-rich: even the outer field, located at ∼17 effective radii of the bulge, has a median metallicity [Z/H] ∼ −0.15, and the fraction of stars with [Z/H] < −1.0 is negligible. This is unprecedented among massive galaxy halos studied to date, even among giant ellipticals. We find significant radial metallicity gradients, characterized by an increase in the fraction of metal-poor stars with radius and a gradient in median metallicity of ∼0.01 dex kpc^{-1}. The density profile is well fit by power laws with slopes that exhibit a dependence on metallicity, with flatter slopes for more metal-poor stars. We discuss our results in the context of recent stellar MDF studies of other nearby galaxies and potential formation scenarios for the Sombrero galaxy.

Unified Astronomy Thesaurus concepts: Galaxy stellar halos (598); Galaxy spheroids (2032); Metallicity (1031); Star formation (1569); Galaxy stellar content (621)

1. Introduction

Stellar population gradients in the external regions of galaxies serve as powerful diagnostic tools to constrain their formation histories. Massive early-type galaxies were found to be consistent with the global relationship between halo metallicity and luminosity found for disk galaxies (Mouhcine et al. 2005a), indicating that such a relationship persists regardless of galaxy type. Recent simulations predict a halo mass–metallicity relation (D'Souza & Bell 2018; Monachesi et al. 2019), confirmed by observations of Milky Way–mass disk galaxies despite a rich diversity in the resolved stellar population properties of their halos (Harmsen et al. 2017). For these late-type galaxies, the simulations reveal that such a correlation is a consequence of the mass–metallicity relation of the disrupted dwarf satellites contributing to their halos, consistent with the detection of substructure. Furthermore, density and metallicity gradients (and their scatter) encode information about the mass and time of accretion of the dominant progenitor (D'Souza & Bell 2018). In particular, galaxies with fewer significant progenitors have more massive halos and steeper negative halo metallicity gradients and density profiles (Monachesi et al. 2019).

Such a plethora of recent insights into the assembly histories of late-type galaxies was facilitated by *Hubble Space Telescope* (*HST*) imaging campaigns of their halos (e.g., Mouhcine et al. 2005b; Radburn-Smith et al. 2011), resolving individual stars on the red giant branch (RGB) to measure metallicity distribution functions (MDFs) photometrically. However, for massive early-type galaxies, imaging suitable for resolved stellar population studies of their halos is still scarce and confined to NGC 5128 (Cen A; Rejkuba et al. 2014, and references therein) plus four additional E and S0 galaxies (Harris et al. 2007a, 2007b; Mould & Spitler 2010; Peacock et al. 2015; Lee & Jang 2016). Information on density and metallicity gradients in massive early-type galaxies is crucial for comparisons to models, which predict a higher accreted mass fraction than late-type galaxies at fixed mass, as well as a fraction of accreted material that increases with total galaxy mass (Cooper et al. 2017; D'Souza & Bell 2018). In particular, simulations predict that the duration of accretion is a function of galaxy mass such that massive early-type galaxies have accreted most of their material by $z \sim 2$ (Oser et al. 2010).

Observations of massive early-type galaxies thus far appear to be in accord with the two-phase formation scenario and its dependence on mass. This is evidenced by uniformly old ages for more massive early-type galaxies (Greene et al. 2013; Young et al. 2014; McDermid et al. 2015; Guérou et al. 2016), along with shallower metallicity gradients compared to both lower-mass early-type galaxies (Pastorello et al. 2014; Greene et al. 2019) and more massive late-type galaxies (Goddard et al. 2017; Li et al. 2018). However, nearly all of these observations, employing integrated light, are restricted to the inner few effective radii ($R_{\rm eff}$) of their target galaxies (see, e.g., Table 5 of Goddard et al. 2017), whereas accreted material likely dominates only beyond ∼20 kpc (Cooper et al. 2015). Indeed, the *HST* imaging campaign of the halo of NGC 5128 at increasingly large distances (Rejkuba et al. 2014, and

* Based on observations made with the NASA/ESA *Hubble Space Telescope*, obtained at the Space Telescope Science Institute, which is operated by the Association of Universities for Research in Astronomy, Inc., under NASA contract NAS 5-26555. These observations are associated with program GO-14175.

Table 1
Sombrero Galaxy Minor-axis Halo Fields

Instrument	R.A. (J2000) (deg)	Decl. (J2000) (deg)	L (deg)	B (deg)	D_{M104} (arcmin)	D_{M104}[a] (kpc)	$E(B-V)$[b] (mag)	t(F606W) (s)	t(F814W) (s)
ACS/WFC	189.9604	−11.4317	298.3805	51.3375	11.69	32.5	0.0385	26150	19960
WFC3/UVIS	189.9862	−11.5301	298.4322	51.2412	5.62	15.6	0.0323	28850	21580

Notes.
[a] Assuming a distance of 9.55 Mpc for M104 from McQuinn et al. (2016).
[b] Schlafly & Finkbeiner (2011).

references therein) demonstrated that the halos of even the most massive early-type galaxies can have a metal-poor contribution, but such a contribution only becomes detectable at very large radii.

The Sombrero galaxy (=M104 = NGC 4594) is an enigmatic stellar system that has often been considered to exhibit an archetypal classical merger-built bulge (Kormendy & Kennicutt 2004, and references therein). It is both nearby ($d = 9.55$ Mpc; McQuinn et al. 2016) and massive, with a total stellar mass of $\sim 2 \times 10^{11}\ M_{\odot}$ (e.g., Tempel & Tenjes 2006; Jardel et al. 2011). It is viewed nearly edge-on (inclination $\sim 84°$; Emsellem et al. 1996), displaying spectacular dust lanes in the plane of a disk hosting very low level ($0.1\ M_{\odot}\ \mathrm{yr}^{-1}$) star formation (Li et al. 2007). Formally classified as type Sa (de Vaucouleurs et al. 1991), the nature of the Sombrero galaxy is currently controversial, due largely to the extended spheroid revealed by 3.6 μm imaging from the *Spitzer Space Telescope*, in addition to multiple inner rings or disks. In particular, two-dimensional multicomponent fits to the *Spitzer* imaging by Gadotti & Sánchez-Janssen (2012, hereafter GSJ12) were significantly improved when an exponential halo was included as a third component in addition to a bulge and disk. The inclusion of the halo as a third component drastically affects the structural parameters of the system, lowering the effective radius of the bulge by a factor of seven to 0.46 kpc (along the major axis), halving the bulge Sérsic index from $n \sim 4$ to 2, and decreasing the bulge-to-total ratio B/T from 0.77 to 0.13.

These dramatic changes are particularly intriguing when placed against the backdrop of known scaling relations for different galaxy types. When the spheroid is included in the fit, the location of the bulge in the mass–size relation becomes inconsistent with elliptical galaxies, lying much closer to the loci of bulges and pseudobulges, although in both cases it is somewhat small for its mass. On the other hand, the smaller bulge from the three-component fit, taken at face value, would imply a black hole mass discrepant by about an order of magnitude from the relation between bulge mass and black hole mass, but including the spheroid in the mass estimate alleviates this discrepancy (GSJ12). Furthermore, when the spheroid is taken alone, the fits of GSJ12 give an effective radius of 3.3 kpc, placing it in excellent agreement with the loci of elliptical galaxies, not bulges, in the mass–size relation. The similarity of the spheroid to elliptical galaxies is underscored by its spectacular globular cluster (GC) population, since the specific frequency of GCs (S_N, which is a measure of the number of GCs per unit galaxy luminosity in the V band) is discrepant with *any* values seen for disk galaxies, regardless of whether the spheroid is considered separately, but is in good agreement with values seen for elliptical galaxies (Rhode & Zepf 2004; Maybhate et al. 2010). Meanwhile, GSJ12 demonstrate in their Figure 12 that the Sombrero is an outlier in several galaxy scaling relations versus mass. However, when the disk component from the three-component fits is considered alone, the Sombrero disk appears reasonably typical of spiral galaxies. In summary, we are left with a situation where the spheroid and disk, considered separately, seem fairly typical of elliptical and spiral galaxies, respectively. However, taken together, the Sombrero as a whole does not appear typical of spirals, lenticulars, or ellipticals. In this context, further insight into the nature of the spheroid is key to resolving the formation history of the Sombrero, with the goal of discriminating whether it bears a closer resemblance to multi-component halos of Milky Way–mass disk galaxies or massive elliptical galaxies.

The remainder of this study is organized as follows: In the next section, we describe our observations and data reduction. Our technique for deriving a photometric MDF is explained in Section 3, and the resulting MDFs and radial density profiles are presented in Section 4. In Section 5 we compare our results with other nearby massive galaxies and predicted formation scenarios for the Sombrero, and in the final section we summarize our results.

2. Data

2.1. Observations

The observations we analyze consist of simultaneous *HST* imaging of two fields located approximately along the minor axis of the Sombrero, obtained in coordinated parallel mode (GO-14175, PI: P. Goudfrooij). Specifically, a WFC3/UVIS field located at 15.6 kpc and an ACS/WFC field at 32.5 kpc from the center of M104 were imaged between 2016 May 18 and June 14 in the F606W and F814W filters of each instrument by obtaining 52 individual exposures (32 in F606W and 20 in F814W) per instrument. The individual exposures were divided into three categories, with 5 (2) short exposures of 250–310 s each, 15 (6) medium exposures of 600–700 s, and 12 (12) long exposures of 1315–1400 s in F606W (F814W), with individual exposure times varying slightly depending on instrument. The locations of the two fields and their total exposure times are summarized in Table 1.[7]

In the left panel of Figure 1, we show the location of the ACS and UVIS fields, overplotted in red on a DSS image of M104. We also show in green the shallower ACS and UVIS fields from GO-13804, a subsection of which was used to measure a tip of the red giant branch (TRGB) distance to M104

[7] The *HST* data used in this work are available at MAST at 10.17909/t9-8daq-vr76.

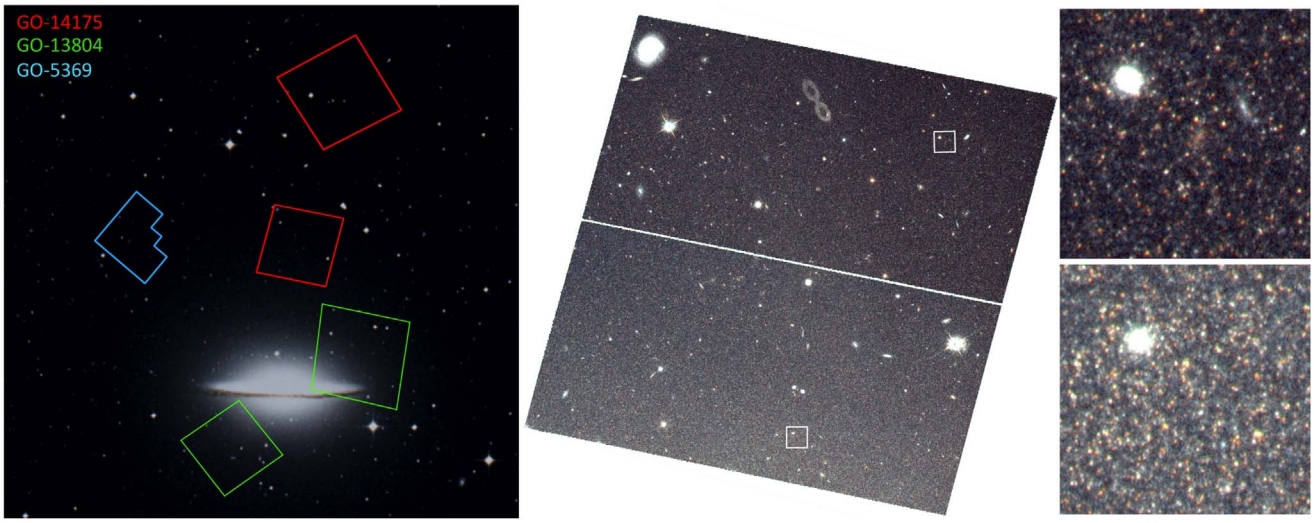

Figure 1. Left: Footprints of recent *HST* imaging of M104. The two fields analyzed here are shown in red; the shallower fields observed in GO-13804, including the field used to measure a TRGB distance by McQuinn et al. (2016), are shown in green; and the shallow WFPC2 field used to infer an MDF by Mould & Spitler (2010) is shown in cyan. Middle: three-color image of our UVIS field at ∼16 kpc along the minor axis, constructed by using the deep drizzled F606W and F814W images for the blue and red channels, respectively, and the average of the two for the green channel. The stellar density gradient with distance from M104 is immediately apparent. Right: zoomed-in color images of the two fields indicated by white boxes in the middle panel to highlight the stellar densities at different locations. Each image is 10′ on a side, and the top and bottom images contain the globular clusters RZ3174 and RZ3026, respectively (Dowell et al. 2014, and references therein) in the upper left corner. In all panels, north is up and east is to the left.

by McQuinn et al. (2016), as well as the WFPC2 field used to obtain an MDF by Mould & Spitler (2010) in blue.

2.2. Preprocessing and Photometry

To create a deep stacked distortion-corrected reference image for each filter, we started from the `.flc` files provided by the `calacs` or `calwfc3` pipeline. The `.flc` files constitute the bias-corrected, dark-subtracted, and flat-fielded images and include corrections for charge transfer inefficiency. First, we aligned all the `.flc` files for a given filter to each other, adopting the first exposure as the reference frame, using the software TWEAKREG, part of the *Drizzlepac* package (Gonzaga et al. 2012). The transformations between the individual images are based on the fitted centroid of hundreds of stars on each image, and the solution was refined through successive iterations, providing an alignment of the individual images to better than 0.04–0.05 pixels. Then, to remove the geometric distortion, correct for sky background variations, flag and reject bad pixels and cosmic-rays, and combine all the different individual exposures, we used the software *AstroDrizzle*, also part of the *Drizzlepac* package. The final stacked images were generated at the native resolution of WFC3/UVIS and ACS/WFC (i.e., $0\farcs040$ pixel^{-1} and $0\farcs049$ pixel^{-1}, respectively).

With a deep, drizzled, distortion-corrected reference image in hand for each field, subsequent preprocessing and photometry of individual science images for each field were performed using version 2.0 of the publicly available `Dolphot` package[8] (Dolphin 2000). Preprocessing was carried out according to the recommendations of each (instrument-specific) `Dolphot` manual, including masking bad pixels, separating each science image into individual chips for photometry, and calculating the sky background.[9]

`Dolphot` uses customized point-spread functions (PSFs) tailored to each filter of each *HST* instrument to perform iterative PSF photometry simultaneously across multiple science images that are aligned positionally to the deep distortion-corrected reference image. After experimentation with numerous reduction strategies, we decided to perform a single `Dolphot` run on all images in both filters for each chip of each instrument. By comparing completeness limits, photometric errors, and color and magnitude offset (bias) as a function of color–magnitude location across test runs, we found that `Dolphot` runs that were separated by filter and/or exposure length and then matched a posteriori yielded results that were similar or inferior to performing a single run per detector chip on all 52 images.

Many optional parameters governing how image alignment, PSF fitting, and sky subtraction are performed may be altered within `Dolphot`, and in cases of severe stellar crowding, modifying these parameters can result in deeper, more complete photometric catalogs (e.g., Williams et al. 2014; Cohen et al. 2018b). Therefore, we adopt the parameters used by Williams et al. (2014) given the crowded nature of our fields (e.g., Dong et al. 2017; Conroy et al. 2018). This set of `Dolphot` parameters includes setting `Force1` = 1, which effectively trades away the ability to use the Object Type parameter for star–galaxy discrimination in exchange for deeper, more complete photometry. Therefore, this choice requires judicious use of several photometric quality diagnostics output by `Dolphot` to cull nonstellar sources (including image artifacts, background galaxies, and GCs) from our catalogs. The photometric quality diagnostics included in the raw catalogs output by `Dolphot` include the shape parameters `sharp` and `round`, signal-to-noise ratio (S/N), the `crowd` parameter indicating how much brighter each star would have been (in magnitudes) had it not been simultaneously fit with its neighbors, and the χ^2 of the PSF fit. For each star, these parameters are given per image, per filter (combined values for

[8] http://americano.dolphinsim.com/dolphot/

[9] We use the high-resolution `step` = 4 value for generating sky frames.

all images of a given filter), and per star (combined values for all images in all filters).

The measurement of photometric metallicities requires accurate color information and accurate magnitude information, so we apply photometric quality cuts to the per-filter values in order to require high-quality imaging in both bands. Our per-filter photometric quality cuts are based on two primary criteria. The first is examination of the recovered values for input artificial stars over a range of position (i.e., projected stellar density), color, and magnitude (see below), under the hypothesis that the loci in (recovered) parameter space that are devoid of artificial stars should be occupied only by nonstellar or spurious sources in the raw observed catalogs (e.g., Cohen et al. 2018b). The second criterion is examination of observed sources passing and failing a proposed set of quality cuts in both position–color–magnitude space and visual inspection of accepted and rejected sources in the deep drizzled reference images to ensure that artifacts such as diffraction spikes are completely eliminated. Ultimately, sources retained in our final catalog were required to have $S/N \geqslant 5$, $\texttt{crowd} \leqslant 0.5$, $\chi^2 \leqslant 2$, $|\texttt{sharp}| \leqslant 0.3$, and a photometric quality flag $\leqslant 2$ for each of the two filters. In addition, we found that contamination by compact background galaxies was drastically reduced using a cut on $|\texttt{sharp}|$ versus magnitude in each filter by fitting a hyperbolic equation of the form $|\texttt{sharp}| < A + Bexp(m - C)$ (Mihos et al. 2018; Durrell et al. 2010). Here, m corresponds to the magnitude in each filter, and we solve for the coefficients A, B, and C using nonlinear least-squares fits to the 99.5% envelope (calculated in 0.1 mag bins) of recovered $|\texttt{sharp}|$ for the artificial stars.

The magnitudes output by Dolphot are calibrated to the Vegamag system using the encircled energy corrections and photometric zero-points from Bohlin (2012) for ACS/WFC and from Deustua et al. (2016, 2017) for WFC3/UVIS. For each field, the photometric catalogs were corrected for foreground extinction using the Schlafly & Finkbeiner (2011) recalibration of the Schlegel et al. (1998) reddening maps and the extinction coefficients given in Casagrande & VandenBerg (2014, their Table A1). These maps reveal low foreground extinction of $E(B-V) < 0.05$ for all of the sight lines analyzed here. All of the magnitudes and colors we report are in the ACS/WFC Vegamag system, corrected for foreground extinction. For the UVIS field, foreground-extinction-corrected magnitudes were transformed to the ACS/WFC photometric system using the empirical relations of Jang & Lee (2015). We note that the uncertainties on these transformations are ∼0.01 mag, negligible compared to our photometric errors (ascertained via artificial star tests) of ∼0.1 mag even at the metal-poor TRGB. The color–magnitude diagrams (CMDs) of each of the two target fields are shown in Figure 2.

Artificial star tests were performed, also using Dolphot, to quantify incompleteness and photometric errors and offsets in our catalogs. In order to reliably sample these quantities over the full range of observed values, hundreds of thousands of artificial stars were generated for each field. To ensure realistic consideration of the effects of blending and crowding, as well as the necessary spatial and color–magnitude coverage, artificial stars were assigned F814W magnitudes drawn from an exponential luminosity function (e.g., Nataf et al. 2013), noting that inserting artificial stars down to more than 3 mag faintward of our 50% completeness limits (F814W ∼ 31) allows us to quantify the effects of blending on our observed catalog. Artificial stars were assigned colors to densely sample the color–magnitude distribution of stars with metallicities ranging from −2.5 to 0.5, including additional scatter of >0.1 mag in color and magnitude to account for uncertainties in distance, reddening, and photometric zero-points plus model-to-model variations in isochrone predictions. The artificial stars were assigned an input spatial distribution corresponding to a power-law density profile with power-law exponent ∼ −2 based on the surface brightness profile of GSJ12 and the GC density profile of Moretti et al. (2003). Artificial stars were photometered one at a time so that they are susceptible to crowding effects from real stars but not from other artificial stars, and they were considered recovered if they passed all of the quality cuts described above.

In Figure 3 we plot completeness versus magnitude for both filters of both instruments, illustrating the strong dependence on color (left panel) and a more modest dependence on projected stellar density, varying with distance from M104 (middle panel). These trends illustrate the necessity to use a large number of artificial stars to fully map incompleteness as a function of all three of these observables (color, magnitude, and projected density). In addition to incompleteness, photometric errors and bias must be similarly mapped over the entire CMD region of interest in order to translate our observations to the true MDFs from which they are generated.

3. Analysis

3.1. Strategy

Using resolved stellar photometry of the upper RGB to measure MDFs photometrically has the advantage that at high S/N, location on the CMD is relatively sensitive to changes in metallicity compared to photometric errors. However, the exact interplay between observational uncertainties and the resulting uncertainties on photometric metallicity depends on a combination of stellar parameters (metallicity itself, luminosity, temperature, and to a lesser extent α-enhancement and age) plus observational effects (i.e., photometric errors and offsets as a function of color, magnitude, and crowding). While photometric MDF analyses often assume that photometric errors are Gaussian, or their influence on metallicity (in terms of either Z or log Z) is Gaussian, there are three ways in which this oversimplification can quantitatively affect the resulting MDF, particularly at low to moderate S/N, as is the case for our observations:

1. Color and magnitude errors are almost always correlated, especially for crowding-limited imaging. This correlation generally functions advantageously, in that the sense of the correlation serves to scatter stars more parallel to the isochrones rather than orthogonally, although the extent to which this is the case depends on CMD location. This is illustrated in the left panel of Figure 4, where photometric errors from artificial star tests are plotted in the sense of recovered-input magnitude in each box, analogous to the scattering kernels of Brown et al. (2009). A subset of 12 Gyr solar-scaled BaSTI isochrones (Pietrinferni et al. 2004, 2006) are overplotted in purple, increasing in metallicity from left to right.
2. At low to moderate S/N, there is a mean offset (bias) between input and recovered color and magnitude, and this effect worsens with decreasing S/N and increased crowding. This is seen in the left panel of Figure 4, where

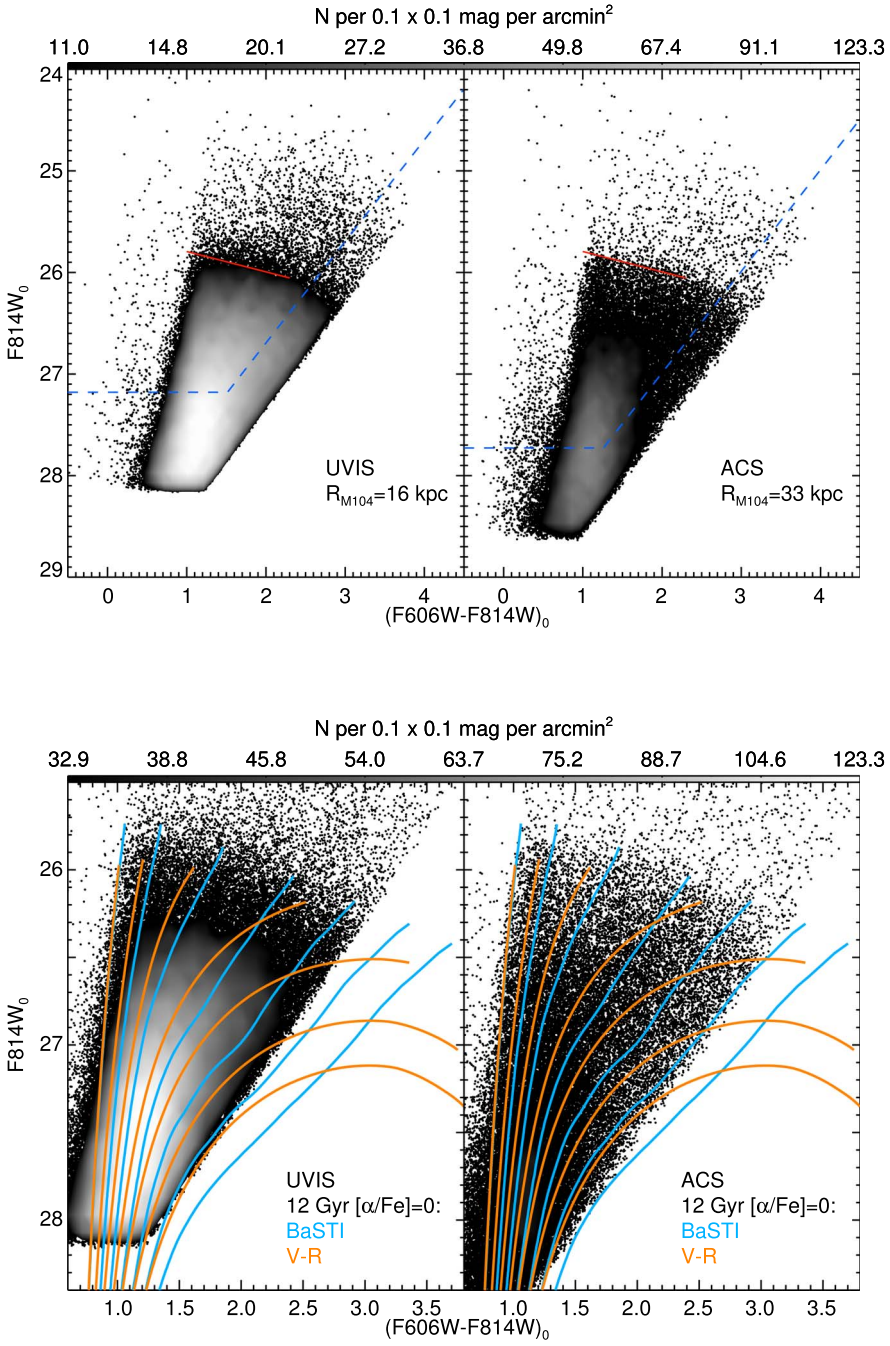

Figure 2. Top: CMDs of the UVIS (left) and ACS (right) target fields, where the color scale indicating density according to the color bars has been held fixed between the two fields to enable a direct comparison. The 50% completeness limits are indicated by a dashed blue line, and the TRGB measured by McQuinn et al. (2016) assuming the Rizzi et al. (2007) calibration is shown as a solid red line. Photometry has been corrected for foreground extinction (Schlafly & Finkbeiner 2011), and UVIS magnitudes have been transformed to the ACS/WFC photometric system (Jang & Lee 2015). Bottom: same as the top panel, but zoomed in on the Sombrero RGB with 12 Gyr solar-scaled BaSTI (cyan) and Victoria-Regina (orange) isochrones with [Z/H] = [−2.3, −1.0, −0.52, −0.20, 0, 0.18, 0.31] overplotted assuming $(m - M)_0 = -29.90$ (McQuinn et al. 2016).

the observed photometric error distributions are shown for a set of CMD locations, each compared to a null offset between input and recovered magnitudes indicated by the dotted blue lines. Furthermore, it is apparent that at low S/N, the photometric error distributions become inconsistent with a bivariate Gaussian, even once the correlated nature of color and magnitude errors is accounted for.

3. The previous two effects often conspire to render the distribution of metallicity error non-Gaussian. This is shown in the right panel of Figure 4 for four CMD locations. For each of the four example CMD loci, there are three plots: The lower plot shows the photometric error distribution ascertained from artificial star tests (as in the left panel), and the mean spatially integrated color and magnitude biases and their uncertainties are reported, highlighting that these biases are statistically significant, nonnegligible in amplitude, and highly sensitive to CMD location (and also, though not shown here, crowding, as revealed by a comparison between biases in the UVIS and ACS fields at the same CMD locations.) The upper

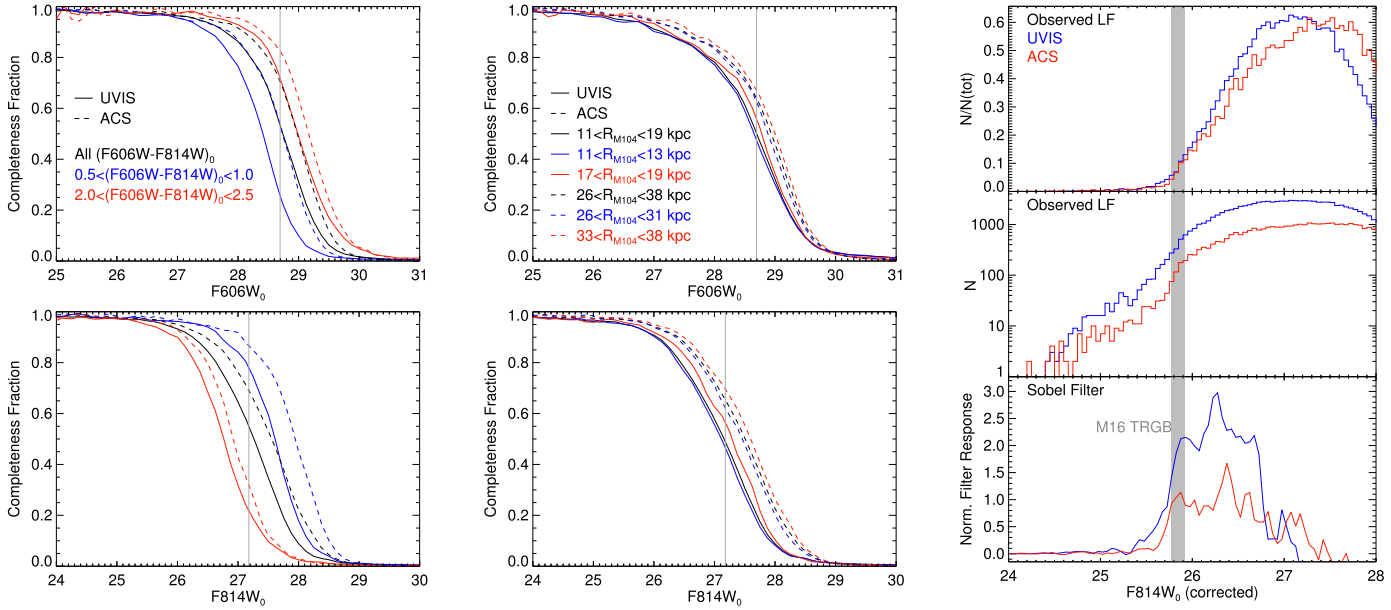

Figure 3. Left: completeness vs. magnitude in the F606W (top) and F814W (bottom) filters, where solid lines correspond to the UVIS field and dashed lines correspond to the ACS field. Completeness curves are color-coded by $(\mathrm{F606W}-\mathrm{F814W})_0$ color as indicated in the top panel to highlight the dependence of completeness on color at fixed magnitude. The vertical gray line indicates the UVIS 50% integrated completeness limit adopted for our analysis. Middle: same as the left panels, but illustrating the dependence of completeness on stellar density for each field using two nonneighboring radial bins. Right: observed luminosity functions for our two target fields using $\mathrm{F814W}_0$ magnitudes corrected for the color dependence of the TRGB (Rizzi et al. 2007) and colors $1 \leqslant (\mathrm{F606W}-\mathrm{F814W})_0 \leqslant 2.3$. The top two panels show the observed LFs on linear normalized and logarithmic y-axis scales to demonstrate the similarity between the two fields in the vicinity of the TRGB, and the bottom panel shows the Sobel filter response. The brightest Sobel filter peak in both fields is in good agreement with the TRGB magnitude reported by McQuinn et al. (2016), indicated by the shaded gray region (including both statistical and systematic errors). The slight broadening of the UVIS LF near the TRGB and its brighter normalized LF peak at the faint end are due to lower completeness caused by increased crowding.

two plots corresponding to each CMD location show histograms of recovered-input metallicities (shown versus $[\mathrm{Z/H}] = \log Z/Z_\odot$ in the upper left panel and versus Z in the upper right panel) based on interpolation between the isochrones. While it may not be surprising that some of the resulting distributions of metallicity error are non-Gaussian, two subtleties deserve mention: First, the CMD locations with relatively Gaussian, symmetric photometric error distributions can yield substantially non-Gaussian distributions of metallicity error, and vice versa. Second, whether asymmetric photometric error distributions map to asymmetric distributions in [Z/H] and/or Z depends on the *combination* of CMD location and observational effects. The implication is that any assumption on the functional form of either the photometric error distribution or the metallicity error distribution cannot safely be assumed as valid over the entire sample CMD region. Therefore, the direct use of a large number of artificial stars is required for a proper characterization of photometric errors and bias as a function of color, magnitude, and projected stellar density.

Considering these effects, realistic attempts to recover MDFs and estimate their uncertainties from low- to moderate-S/N photometry require forward modeling of CMDs. This stems from the fact that even when extensive artificial star tests are available to quantify the aforementioned observational biases, one cannot "unscatter" observed colors and magnitudes on a star-by-star basis. In other words, with only output photometry available for the observed sample, the metallicity distribution one obtains by simply interpolating in an isochrone grid on a star-by-star basis will be sensitive to the assumed input artificial star distribution. To alleviate this issue, we take the approach of forward modeling the CMD as a linear combination of simple stellar populations (SSPs). In general, this procedure comes at the cost of sacrificing a strictly continuous metallicity distribution to instead obtain a piecewise one composed of various SSPs. However, in the present case this cost is essentially nullified since our photometric errors result in 1σ metallicity uncertainties of $\gtrsim$0.15 dex even where the metallicity resolution is highest, and several times worse over much of the M104 RGB, evident in the right panels of Figure 4.

3.2. Maximum Likelihood Fitting of CMDs

We implement forward modeling of observed CMDs for each field using the star formation history code StarFISH (Harris & Zaritsky 2001, 2012). We assume an age of 12 Gyr based on spectroscopy of GCs in the Sombrero (Larsen et al. 2002; Hempel et al. 2007). The CMDs are assumed to be a linear combination of solar-scaled isochrones, and in order to investigate the effects of model-to-model variations, we include both BaSTI models and Victoria-Regina (V-R; VandenBerg et al. 2014) models.[10] For each isochrone set, we employ 16 12 Gyr isochrones with $-2.30 \leqslant [\mathrm{Z/H}] \leqslant +0.31$ spaced such that $\Delta Z/Z \leqslant 1$, and a subset of these isochrones are shown in the bottom panel of Figure 2. In the presence of large photometric errors, too fine a metallicity sampling can result in large correlated uncertainties between isochrones that are photometrically degenerate, so to alleviate this issue while maintaining a useful metallicity resolution, StarFISH gives the option to lock subsets of isochrones together, meaning that

[10] We also used BaSTI models with $[\alpha/\mathrm{Fe}] = +0.4$ for comparison purposes but found that the results were indistinguishable when expressed in [Z/H].

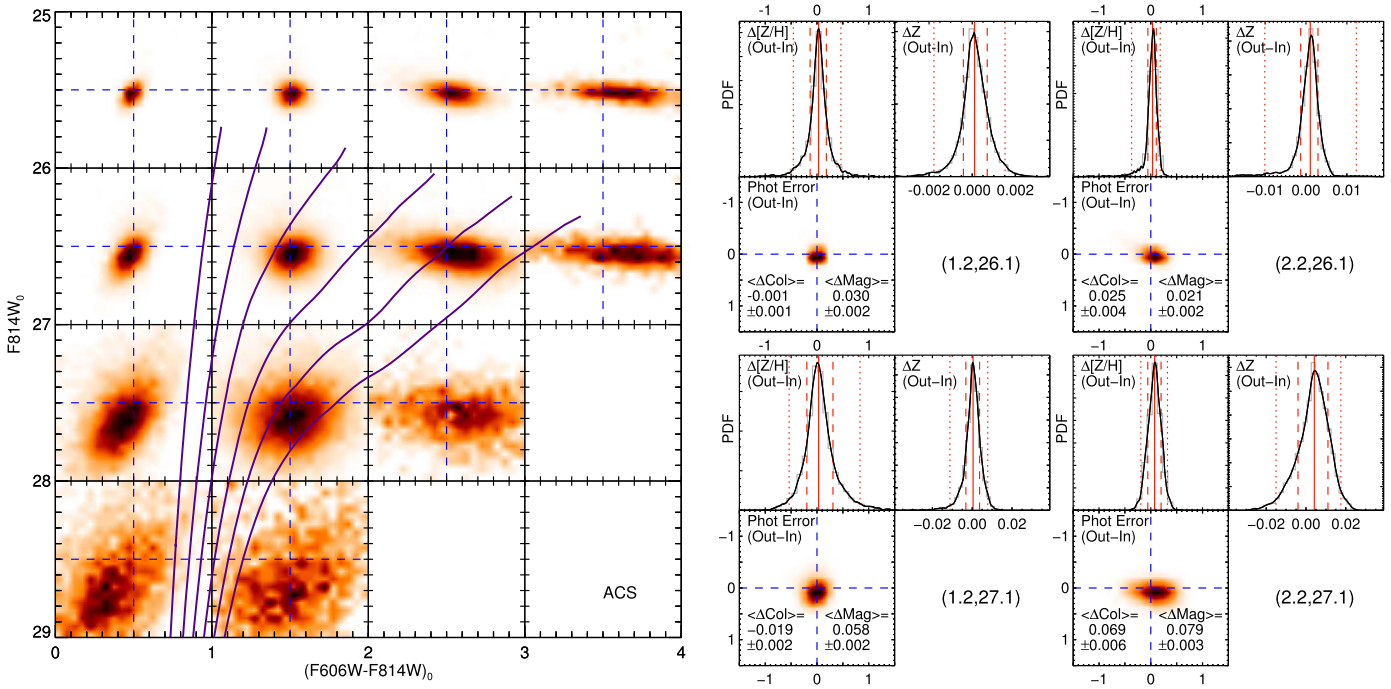

Figure 4. Left: photometric errors as a function of CMD location for the example case of the ACS field, evaluated using artificial star tests. For each CMD box, color and magnitude errors are plotted in the sense (recovered-input). Solar-scaled 12 Gyr BaSTI isochrones from $-2.3 \leqslant$ [Z/H] $\leqslant +0.3$ (only shown through the RGB tip for clarity, identically to Figure 2) are overplotted in purple. Right: for four example CMD locations (given in the lower right of each set of plots), the lower plot shows the photometric error distribution in the same way as the left panel, and the mean biases (offset) in color and magnitude are given, along with their uncertainties. The upper plots show the difference between output and input *metallicity*, also in the sense (recovered-input), as a function of global metallicity [Z/H] = log ($Z/Z_\odot$) (upper left) and heavy-element abundance Z (upper right). The gray histogram displays the raw values, the black line displays the density function obtained using kernel density estimation, and the vertical red solid, dashed, and dotted lines display the median offset and 1σ and 2σ intervals, respectively.

the amplitudes of isochrones in a locked subset (i.e., neighboring each other in metallicity) are constrained to vary together in lockstep. After experimenting with various strategies to determine which yields the highest-quality fits while minimizing correlated errors in the SSP amplitudes of the solution, we employ nine locked subsets of isochrones. In addition, we allow the amplitude of the foreground plus background contamination model (see Section 3.3.2) to vary, for a total of 10 SSP amplitudes fit to each CMD. We assume a Salpeter initial mass function (IMF) and a binary fraction of 50%, although these choices have a negligible effect on our results since the stellar mass range that may populate our CMD is quite small, <25% across the entire sampled metallicity range including post-TRGB evolution, but <1% at fixed metallicity among RGB stars, which dominate the sample.

For each field, our CMD fitting is restricted to stars lying within the region defined by several CMD cuts. Stars are only included in the CMD fitting if they meet the following criteria:

1. F814W$_0 \leqslant 27.18$, which is the 50% spatially integrated F814W completeness limit from the UVIS field (shown in Figures 2 and 3). For consistency, we apply this same limit to the ACS field despite its fainter completeness limit. While many MDF studies employ completeness limits in both filters (Harris et al. 2007a; Mould & Spitler 2010), we found that such a cut sacrificed our ability to meaningfully constrain the most metal-rich (solar to supersolar) population, while yielding consistent results for the remainder of the (subsolar metallicity) sample. Conversely, making a cut using only one filter (e.g., Peacock et al. 2015) has the advantage of yielding statistically meaningful constraints on the supersolar metallicity population provided that extensive artificial star tests have been used to model the variation of incompleteness, photometric error, and bias as a function of color, magnitude, and projected stellar density.
2. (F606W − F814W)$_0 \geqslant 0.5$. This cut eliminates CMD regions where contamination by background galaxies is fractionally large and a negligible fraction (<1%) of even the most metal-poor ($Z = 0.0001$) stars are expected based on the artificial star tests and isochrones.
3. F814W$_0 \geqslant 26$. This cut eliminates candidate RGB and AGB variables not represented in the SSP models, likely due to their large amplitudes and long periods that we are sampling stochastically. This issue is discussed further in the Appendix.

STARFish calculates the best-fit amplitudes evaluated using the Dolphin Poisson statistic (Dolphin 2002) and accounts for correlated uncertainties among the SSPs. However, because the CMD fitting procedure functions by drawing a finite number of artificial stars, binning the CMD and the artificial star error distributions, the total uncertainties we report are the quadrature sum of those from several individual sources (e.g., Hidalgo et al. 2011; Bernard et al. 2018). The first source of uncertainty we consider in the SSP amplitudes is the mean $\pm 1\sigma$ errors reported by STARFish over many repeated runs on each field using the same parameters (i.e., CMD binning) and changing only the random seed. This is necessary to account for stochastic fluctuations stemming from the fact that STARFish uses binned cumulative distribution functions to store crowding and photometric error information over the CMD, and it accounts for variations stemming from a finite number of artificial stars populating each isochrone according

to draws from a prescribed IMF. Because this mean observed uncertainty is with respect to the best-fit amplitude in each run, the second source of error we add in quadrature is the 1σ (calculated as the 16th and 84th percentiles) variation in the mean amplitude for each SSP over all of the runs in which only the random seed is varied. Next, we perform another set of runs on each field, but this time varying both the sizes of the CMD bins and the bin locations for each size in order to account for any biases caused by a particular binning scheme. In particular, the bin sizes are varied by $\pm 80\%$ from our default value of 0.05 mag CMD pixels binned 2×2 to as small as 0.06 mag (0.03 mag CMD pixels binned 2×2) and as large as 0.18 mag (0.06 mag CMD pixels binned 3×3), and for each bin size, the bin starting point is shifted in increments of 0.01 mag in color and magnitude. As a result, we also add in quadrature the $\pm 1\sigma$ variations in the mean amplitude for each SSP over these bin variations, plus any difference between the mean amplitude from the original runs and the mean amplitude from the runs allowing for bin variations. Of the aforementioned sources of error, reassuringly, the uncertainties output directly by STARFish dominate the total error in the majority (65%) of cases. However, the uncertainty due to varying the size and location of the CMD bins that are compared to the observations is nonnegligible, dominating the uncertainty in 28% of the runs (preferentially for the more crowded UVIS field) and contributing a median of 28% to the error budget.

3.3. Contaminants

When fitting our observed CMDs, we must account for the fact that, even given the CMD cuts mentioned in Section 3.2, the Sombrero RGB is subject to some nonzero contamination by foreground Milky Way stars and background galaxies with star-like PSFs. Also, blends and unresolved star clusters may contaminate our catalogs, and we now describe how these potential sources of contamination are quantified.

3.3.1. Foreground Milky Way Stars

We use the TRILEGAL Galaxy model (Girardi et al. 2005, 2012) to predict the density of foreground Milky Way stars toward each of our two target fields. For each field, we sample an area of 0.01 deg^2 on the sky in each TRILEGAL run and concatenate multiple runs to improve Poisson statistics. We find that the predicted foreground contamination does not vary significantly between our two fields owing to their proximity on the sky, and the majority of the foreground contribution occurs significantly brightward of the Sombrero TRGB: for both fields, we find 6.3 foreground contaminants per arcmin^2 over the entire CMD, but only $1.6/\mathrm{arcmin}^2$ anywhere in the approximate magnitude range of the Sombrero RGB ($\mathrm{F814W}_0 > 25.5$) *before* applying the incompleteness in the target fields. Of these, about $1/4$ are white dwarfs or brown dwarfs, so after applying incompleteness in the target fields as a function of color, magnitude, and location (assuming a homogeneous spatial distribution for the contaminants), the predicted number of *recovered* contaminants with $\mathrm{F814W}_0 > 25.5$ drops to 0.58 (0.63) stars arcmin^{-2} for the UVIS (ACS) field. Given the observed source density of well over 10^3 arcmin^{-2} even in the far reaches of the more sparse ACS field, such a contribution by foreground stars is essentially negligible, although we include it in our contamination model described here.

Table 2
Blank ACS/WFC Fields Used to Assess Background Galaxy Contamination

Field	t(F606W) (s)	t(F814W) (s)	L (deg)	B (deg)
ABELL-2744-HFFPAR	24223	25430	9.15	−81.16
MACS-J1149-HFFPAR	25035	23564	228.57	75.18
ABELLS1063-HFFPAR	24635	23364	349.37	−60.02

3.3.2. Background Galaxies

We build a model describing the distribution of background galaxies predicted using imaging of high Galactic latitude "blank" fields. The construction of the background galaxy CMD distribution is described in more detail in Mihos et al. (2018) and Cohen et al. (2018a) but can be briefly summarized as follows.

First, we searched the *HST* archive for fields far from the Galactic plane (to minimize the impact of foreground stars) observed in identical filters and similar (or deeper) exposure times to those of our science images. This search yielded three fields observed as coordinated parallels in the *HST* Frontier Fields program, described in more detail in Lotz et al. (2017) and listed in Table 2. We then selected a subset of exposures in each of these fields so as to obtain exposure times similar to our Sombrero imaging, mimicking the photometric depth of our observations. We performed `Dolphot` photometry and artificial star tests on these images exactly as described in Section 2.2, including identical photometric quality cuts. The resulting CMD is shown in the top left panel of Figure 5, where sources are color-coded by field. The CMD loci of contaminating background galaxies are essentially identical to what was found in other recent studies employing a similar strategy (Cohen et al. 2018a; Mihos et al. 2018), consisting of a vertical swath of sources with $0 \lesssim (\mathrm{F606W} - \mathrm{F814W})_0 \lesssim 1$ that have a (completeness-corrected) luminosity function rising toward fainter magnitudes. To build our contamination model, we first correct for incompleteness in the blank fields and then apply incompleteness toward our Sombrero fields, resulting in the contamination model shown in the top right panels of Figure 5. Lastly, in the bottom row of Figure 5, we bin the CMD in 0.1×0.1 mag bins to illustrate the *fraction* of sources predicted to be contaminants as a function of CMD location. Here it is clear that the contamination fraction only becomes significant blueward of the metal-poor Sombrero RGB.

3.3.3. Blends

The effect of photometric blends on our imaging can be quantified since we intentionally include artificial stars more than 3 mag faintward of the CMD region used for our analysis, input with a realistic (exponentially increasing toward fainter magnitudes) luminosity function. However, we find that while photometric errors and bias are nonnegligible throughout the observed CMD (see Figure 4), cases where much fainter companions are blended with brighter sources are rare. Over the entire CMD region sampled by the artificial stars, extending down to $\mathrm{F814W} = 31$, less than 1% of sources in the CMD region we employ in either the UVIS or ACS fields had an input magnitude more than 2 mag fainter than its output magnitude. Similarly, of the artificial stars with *output* magnitudes falling in the CMD region we use for our CMD fitting (i.e., brightward of the UVIS 50% completeness limit in

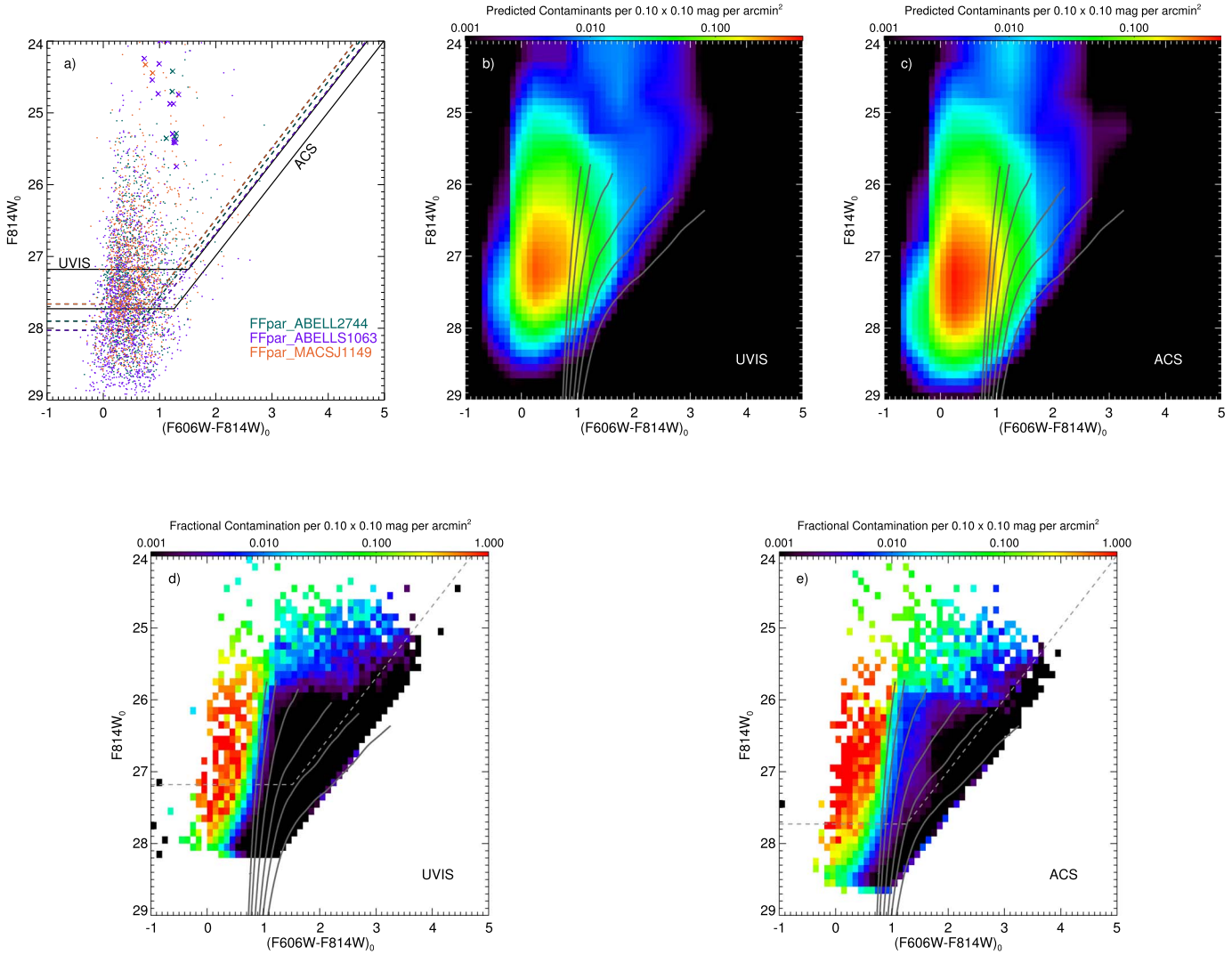

Figure 5. Contamination by background galaxies and foreground Milky Way stars toward our target fields. Top left: sources from the blank galaxy fields passing all of our photometric quality cuts, color-coded by field. Probable foreground stars in each blank galaxy field based on the TRILEGAL model are shown as crosses and excluded from further analysis. The 50% completeness limits in each blank galaxy field are shown as dotted lines, and the 50% completeness limits in our ACS and UVIS target fields are shown as black solid lines. Top middle and top right: Hess diagram of the predicted density of contaminants, including background galaxies plus foreground Milky Way stars toward our target fields, after correcting for incompleteness in the blank Galaxy fields and applying incompleteness in our target fields, for the UVIS and ACS fields, respectively. Curved gray lines represent a subset of 12 Gyr solar-scaled BaSTI isochrones with metallicity $-2.3 \leqslant [Z/H] \leqslant +0.3$ assuming $(m - M)_0 = 29.90$. Bottom row: contamination *fraction* over the CMD for our UVIS (left) and ACS (right) field, shown on a logarithmic color scale.

F814W), less than 0.2% (UVIS) and 0.1% (ACS) had input magnitudes faintward of F814W = 29.

3.3.4. Unresolved Star Clusters

Globular cluster half-light radii range from ∼1 to 10 pc in the Milky Way (Harris 1996, 2010 edition), the inner regions of M104 (Harris et al. 2010), and other massive ellipticals (Woodley & Gómez 2010; Goudfrooij 2012; Webb et al. 2013; Puzia et al. 2014), as well as young massive clusters (Portegies Zwart et al. 2010). At the distance of the Sombrero, 1 ACS/WFC pixel corresponds to 2.3 pc on a side, so that any clusters in our images should be distinguishable from stellar sources, which have a well-defined PSF. For example, Harris et al. (2010) were able to measure GC half-light radii down to ∼0.9 pc (corresponding to 0.″02) using an *HST* mosaic of the inner region of the Sombrero, and they find that there, as in other galaxies (see their Figure 11), the majority of GCs are larger than this, with a distribution of half-light radii peaking at ∼2–3 pc with a tail toward larger sizes. Meanwhile, Spitler et al. (2006) find a Sombrero GC luminosity function that peaks far brightward of the Sombrero TRGB, at $V = 22.17$, and this distribution (see their Figure 3) implies that even in the more central region of the Sombrero targeted by their observations, the projected density of GCs faintward of their completeness limit at $V = 24.3$ is ∼0.1 arcmin^{-2}, so the number of GCs coincident with the Sombrero RGB ($V > 25.5$) in either of our fields is expected to be essentially zero. Furthermore, the radial density profile of Sombrero GCs decreases at increasing projected radii, so given the *stellar* projected densities of our target fields and the size distribution of GCs, the contamination of our fields by GCs is negligible.

4. Results

4.1. Global Metallicity Distribution Functions

Metallicity distributions for the UVIS (16 kpc) and ACS (33 kpc) fields are shown in Figure 6, where error bars

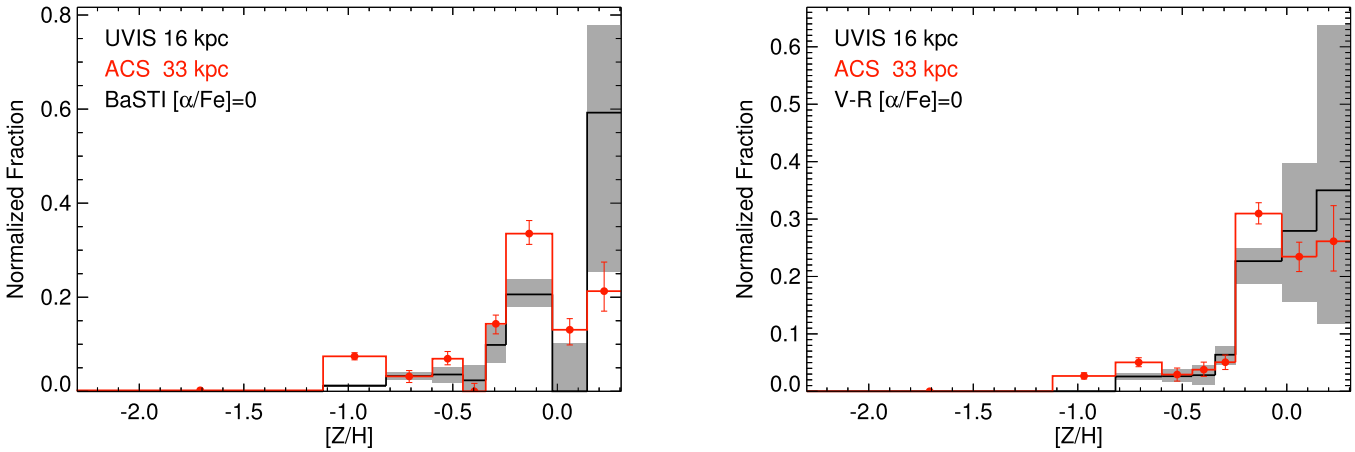

Figure 6. Metallicity distribution functions for the 16 kpc UVIS field, shown in black, with total 1σ uncertainties (calculated as described in Section 3.2) indicated by the gray shaded region, and for the 33 kpc ACS field, shown as a red line with error bars indicating uncertainties. The left and right panels show results based on scaled solar BaSTI and Victoria-Regina models, respectively.

represent the total 1σ uncertainties calculated as described in Section 3.2. Strikingly, both fields are dominated by metal-rich stars, and the most clear difference between them is a decrease in the relative number of supersolar-metallicity stars accompanied by an increased intermediate-metallicity ($[Z/H] \gtrsim -1$) population in the outermost 33 kpc ACS field. The fraction of stars with $[Z/H] < -0.6$ increases by a factor of two to three moving radially outward from the UVIS to ACS fields, and the fraction of stars with $[Z/H] < -0.8$ increases by a factor of six. Focusing on the *relative differences* between the two fields for any set of model assumptions, both isochrone models are in agreement regarding the dominance of metal-rich stars and lack of metal-poor stars. Viewed in terms of a radial gradient in median metallicity, the models concur on a power-law gradient of $\delta[Z/H]/\delta(\log R_{\rm gal}) \sim -0.5$ (or, expressed linearly, ~ -0.01 dex kpc^{-1}), with a median of $-0.06 \leqslant [Z/H] \leqslant 0.03$ in the UVIS field and $-0.19 \leqslant [Z/H] \leqslant -0.12$ in the more distant ACS field. Notably, such a high median metallicity is supported by colors measured from optical integrated light. Hargis & Rhode (2014) present radial color profiles of several early-type galaxies, including the Sombrero, and while their profile extends only to our UVIS field, conversion of their reported colors (and uncertainties) to metallicity using their Equation (4) gives $[Z/H] = -0.03 \pm 0.18$ over the radial range of the UVIS field, in excellent agreement with our results. Perhaps the most striking aspect of the MDFs of the UVIS and ACS fields is the paucity of metal-poor stars, even in the more distant ACS field, where they are relatively more common: of the entire population, both models find that stars with $[Z/H] < -0.8$ constitute less than 10% there. Restricting the entire sample to $[Z/H] < -0.25$, where relative errors are somewhat smaller, stars with $[Z/H] < -0.8$ still constitute less than half and those with $[Z/H] < -1.2$ have 1σ *upper* limits of 1%–4% depending on the adopted isochrone set.

To gain further quantitative insight into the dominance of the metal-rich population and its physical cause via any dependence on projected radius from M104, we divide our sample spatially by projected radius into bins. This division is made by keeping the observed number of stars in each bin similar in an attempt to minimize differences in Poissonian uncertainties across the radial bins, and it is a necessary compromise between spatial (i.e., radial) resolution and number statistics. After testing several radial binning schemes, we employ a total of five radial bins, three in the UVIS field and two in the ACS field. We performed our STARFish MDF analysis completely independently on each radial bin, employing only artificial stars located in the corresponding bin. While this approach comes at the cost of number statistics, it has the advantage of locally sampling the true stellar density in each radial bin, minimizing the effects of (and serving as a check on) a single assumed sample-wide density gradient for the artificial stars. The resulting MDFs for each radial bin (and the radial bin locations) are shown in Figure 7, where we see in more detail the decreasing fraction of supersolar-metallicity stars and the increasing fraction of subsolar-metallicity stars with increasing projected distance from M104 moving from top to bottom in each panel. However, the variation in MDF with projected distance seen in Figure 7 is subtle enough that no statistically significant variations are seen *within* either the UVIS or ACS field in median metallicity or fraction of metal-poor stars.

4.2. Relationship with Density Profiles

The results from Figures 6 and 7 imply the presence of a metallicity-dependent density gradient across the range of projected radii sampled by the imaging. To test for changing projected radial density gradients as a function of metallicity, we now make the opposite trade-off as in Section 4.1, namely, we retain the spatial resolution from the radial bins and search for coarse differences as a function of metallicity. To this end, we select three nonneighboring metallicity ranges and plot their stellar densities in each radial bin in Figure 8. We find that for each of the three metallicity ranges, the power-law slopes agree to within their uncertainties across the three isochrone sets, all finding a metallicity dependence on the power-law density slope such that the more metal-poor population has a flatter density profile while increasingly metal-rich populations have increasingly steep power-law density profiles. Meanwhile, the density profile of the entire stellar sample (with no metallicity cuts), shown using black open circles in Figure 8, has a power-law slope of $\delta(\log \Sigma)/\delta(\log R_{\rm gal}) \sim -2.8 \pm 0.4$ (where Σ denotes the projected stellar density). If we compare this slope to the surface brightness profile of Hargis & Rhode (2014), who fit only Sérsic and $r^{1/4}$ laws, their data give a power-law slope of -2.10 ± 0.01 when fit over their entire radial range. However, restricting the fit to only the radial range occupied by

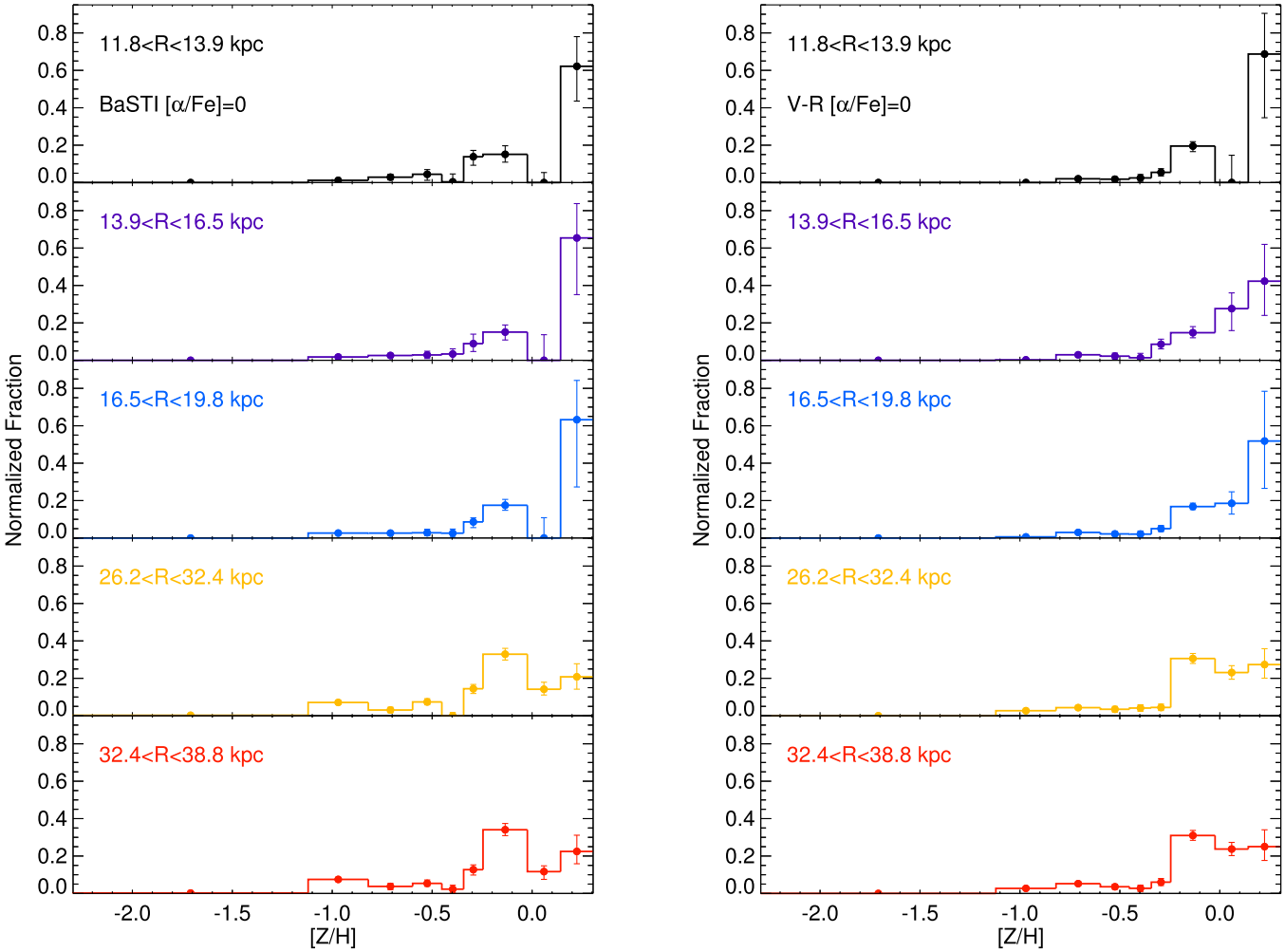

Figure 7. Metallicity distribution functions, normalized to their total. Each column represents a different set of isochrones as in Figure 6, but for each assumed isochrone set we now plot separate MDFs for each radial bin, indicated in each panel, moving farther from the center of M104 from top to bottom in each column.

our fields (in practice, only the UVIS field since they truncate their data at 7′ from the galaxy center), their data result in a power-law slope of -2.70 ± 0.17, in good agreement with our results.

5. Discussion

5.1. Comparison to Other Studies

5.1.1. Previous Results Using WFPC2

The only other study of the stellar MDF of the Sombrero was presented by Mould & Spitler (2010), who studied a field at ∼8′ northwest of the galaxy center using WFPC2 imaging (see Figure 1). They find an MDF peaking at $[Z/H] = -0.5$ with a tail extending to lower metallicities, and the authors acknowledge that the most metal-rich population could have been "erased by incompleteness." While they perform a subset of artificial star tests to measure photometric error and bias in selected color and magnitude ranges, they find that the bias (mean offset between output and input color or magnitude) is small and not statistically significant, and they obtain their MDF by direct interpolation between 12 Gyr isochrones from VandenBerg et al. (2000). However, based on our discussion of the impact of observational uncertainties on the MDF in Section 3.1 illustrated by Figure 4, it is likely that the photometry of Mould & Spitler (2010), which shows significant effects of incompleteness between 1 and 1.5 mag faintward of the TRGB in their Figure 3, may in fact be susceptible to nonnegligible photometric error, bias (and hence metallicity error distribution), and incompleteness varying as a function of color and magnitude across their CMD.

5.1.2. Comparison to Other Nearby Galaxies

In terms of MDFs of halos of other nearby galaxies using resolved RGB stars, there are significant differences between spiral galaxies and early-type galaxies (types E and S0, hereafter ETGs). Starting with the latter, stellar MDFs of halo fields have been derived using *HST* data for a handful of giant ETGs, some of which have measurements for multiple fields at different galactocentric radii. These consist of the S0 galaxy NGC 3115 (Peacock et al. 2015) and the ellipticals NGC 3377 (Harris et al. 2007a), NGC 3379 (Harris et al. 2007b; Lee & Jang 2016), and NGC 5128 (Harris & Harris 2002; Rejkuba et al. 2005, 2014; Crnojević et al. 2013; Bird et al. 2015). Some of these studies also analyzed similar data for nearby lower-luminosity ETGs for comparison purposes (Harris et al. 2007b; Lee & Jang 2016). For halos of spiral galaxies, we use the results of the GHOSTS survey for the edge-on, "normal," $\sim L^*$ spiral galaxies NGC 891, NGC 3031 (= M83), NGC 4565, and

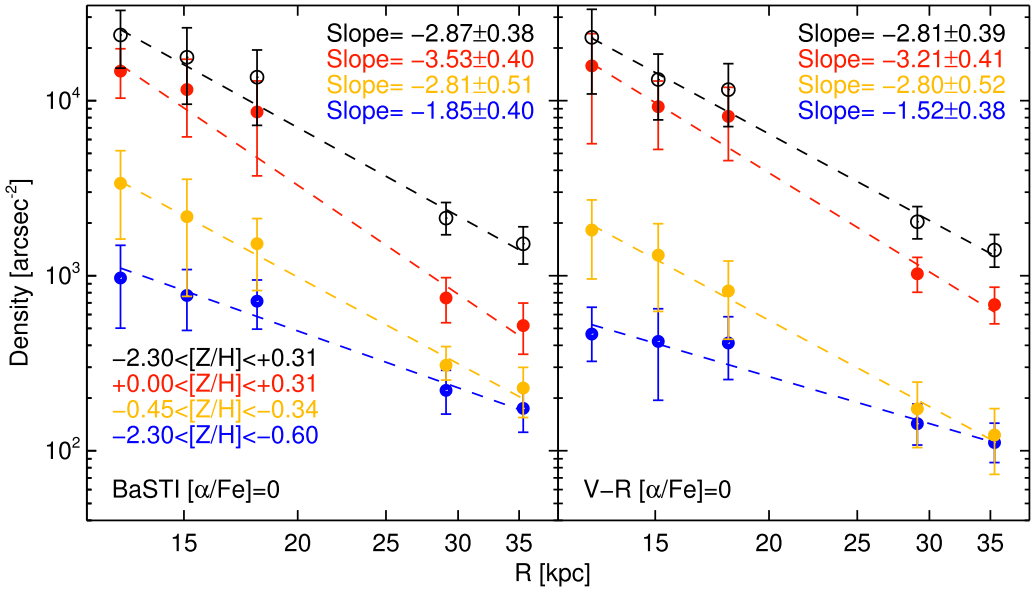

Figure 8. Radial density profiles for stars over the full sampled metallicity range (black open circles) and in three nonneighboring metallicity ranges (given in the lower left corner of the left panel and shown as filled circles color-coded by metallicity) using the same two sets of models as in Figures 6 and 7, after accounting for incomplete azimuthal coverage. Power-law slopes best fitting each density profile are overplotted as dashed lines, and the slopes and their uncertainties are reported in the upper right corner of each panel.

NGC 7814 (Radburn-Smith et al. 2011; Monachesi et al. 2016), in conjunction with results for M31 (Kalirai et al. 2006) and the Milky Way (Ryan & Norris 1991; Mackereth et al. 2019). Relevant data for all these galaxies with stellar MDF data are listed in Table 3. Figure 9 plots the peak [Z/H] (or mode) of the MDF versus M_V^0 for the galaxies in Table 3; ETGs are shown in panel (a), and spiral galaxies are shown in panel (b). Our results on the Sombrero are shown as red pentagons for comparison. Galaxies with MDF data in more than one field are shown with symbol colors other than black, with the symbol size scaled by the galactocentric radius in units of effective radii of the spheroid (or bulge for the spirals), i.e., $R_{\rm gal}/R_{\rm eff}$. For reference, a linear least-squares fit to the data of ETGs with MDF data taken in fields with $R_{\rm gal}/R_{\rm eff} \lesssim 5$ is shown as a dashed line, which has a slope of -0.135 ± 0.035 dex mag^{-1},[11] corresponding to [Z/H] $\propto L_V^{0.34\pm0.09}$.

A number of relevant conclusions can be drawn from Figure 9:

1. Among ETGs, there is a clear correlation between the peak [Z/H] of the halo MDF and the *V*-band luminosity (and, most likely, the mass) of the parent galaxy when considering fields with $R_{\rm gal}/R_{\rm eff} \lesssim 5$. This is thought to reflect a manifestation of the galaxy mass–metallicity relation (see also Gallazzi et al. 2005; Harris et al. 2007b; Kirby et al. 2013; Lee & Jang 2016).
2. Among the sample of nearby galaxies shown in Figure 9, halos of spiral galaxies are typically much more metal-poor (in terms of the peak [Z/H]) than those of ETGs at a given galaxy luminosity. An exception to this is the innermost field of M31 shown in Figure 9, which Kalirai et al. (2006) interpret as being due to a significant contribution of bulge stars.
3. Metallicities among L^* spirals (in terms of both peak [Z/H] and its radial gradient) span a wide range (see also Monachesi et al. 2016). This is in strong contrast to the situation among ETGs: while ETGs with $L \approx L^*$ do show negative radial gradients of [Z/H] (see more on that below), the peak [Z/H] never reaches values <-1.0, even in the distant outskirts of their halos (e.g., the outermost fields in NGC 3115, NGC 5128, and the Sombrero have $17 \lesssim R_{\rm gal}/R_{\rm eff} \lesssim 25$).

Note that in terms of the peak [Z/H] values, the halo fields at $R_{\rm gal}/R_{\rm eff} = 8$ and 17 in the Sombrero are roughly consistent with the trend with galaxy luminosity among ETGs shown in Figure 9, while they are significantly more metal-rich than any luminous spiral galaxy halo with MDF measurements studied to date. Interestingly, this includes NGC 7814, a luminous early-type (Sa) spiral galaxy with a B/T ratio that is very similar to that of the Sombrero, whereas the peak metallicity of the halo of NGC 7814 is a full order of magnitude lower than that of the Sombrero. This is consistent with the finding by Goudfrooij et al. (2003) that the GC population of NGC 7814 has a very low fraction of metal-rich clusters for its B/T ratio relative to the Sombrero.

Moreover, this also seems consistent with the correlation between *halo* mass and metallicity among L^* spiral galaxies in the GHOSTS survey (Harmsen et al. 2017), given the high surface number density of RGB stars in the outer halo of the Sombrero relative to those in the GHOSTS survey. To check this quantitatively, we convert our surface number densities to halo masses between galactocentric radii of 10 and 40 kpc (hereafter M_{10-40}), which Harmsen et al. (2017) found to be a fraction of 0.32 of the total stellar halo mass based on theoretical models. We compute this conversion for RGB stars brighter than our adopted magnitude limit (i.e., $M_{\rm F814W} \leqslant -2.72$) as a function of metallicity using the BaSTI isochrones, adopting an age of 12 Gyr and a Chabrier (2003) IMF. Initial stellar masses were converted to present-day masses using the Bruzual & Charlot (2003) models. Under the assumption of a

[11] Detailed comparisons between MDF studies are hampered somewhat by differences in the analyses (e.g., slightly different CMD regions used to construct the MDF, different isochrone models); the latter typically result in systematic differences in [Z/H] of $\sim$ 0.10–0.15 dex. We have adopted 0.15 dex as the minimum uncertainty of [Z/H] in Figure 9.

Table 3
Peak [Z/H] in MDF of RGB Stars in Halo Fields around Nearby Galaxies

Galaxy (1)	M_V^0 (2)	R_{gal}/R_{eff} (3)	R_{eff} Ref. (4)	Peak [Z/H] (5)	[Z/H] Ref. (6)
		Early-type Galaxies			
UGC 10822	−8.80	2.	M12	−1.74 ± 0.24	H+07b
ESO 410 − G005	−12.45	1.7	P+02	−1.52 ± 0.15	LJ16
NGC 5011C	−14.74	1.5	SJ07	−1.13 ± 0.15	LJ16
NGC 147	−15.60	1.	C+14	−0.91 ± 0.40	H+07b
NGC 404	−17.35	3.5	B+98	−0.60 ± 0.15	LJ16
NGC 3377	−19.89	4.	F+89	−0.41 ± 0.15	LJ16
NGC 3115	−20.83	6.7	F+89	−0.40 ± 0.15	P+15
		14.	F+89	−0.50 ± 0.15	P+15
		21.	F+89	−0.60 ± 0.15	P+15
NGC 3379	−20.83	5.4	F+89	+0.02 ± 0.15	LJ16
		11.8	F+89	−0.15 ± 0.15	LJ16
NGC 5128	−21.29	7.	D+79	−0.20 ± 0.15	R+14
		10.5	D+79	−0.25 ± 0.15	R+14
		15.5	D+79	−0.45 ± 0.15	R+14
		25.	D+79	−0.55 ± 0.20	R+14
NGC 4594	−22.35	8.2	GSJ12	+0.15 ± 0.15	C+20
		17.1	GSJ12	−0.15 ± 0.15	C+20
		Spiral Galaxies			
NGC 7814	−20.67	11.5	F+11	−0.96 ± 0.30	M+16
		17.2	F+11	−1.20 ± 0.30	M+16
		28.7	F+11	−1.40 ± 0.30	M+16
NGC 891	−21.15	5.	F+11	−0.95 ± 0.30	M+16
NGC 3031	−21.18	5.	B+98	−1.23 ± 0.30	M+16
NGC 4565	−21.81	18.	W+02	−1.21 ± 0.30	M+16
		50.	W+02	−1.95 ± 0.30	M+16
M 31	−21.78	10.7	W+03	−0.47 ± 0.03	K+06
		21.4	W+03	−0.94 ± 0.06	K+06
		60.7	W+03	−1.26 ± 0.10	K+06

Note. Galaxies are listed in order of their *V*-band luminosities. Column (1): galaxy name. Column (2): absolute *V*-band magnitude from NED. Column (3): ratio of galactocentric radius of halo field in terms of the effective radius of the galaxy, R_{gal}/R_{eff}. Column (4): reference for R_{eff}: M12 = McConnachie (2012), P+02 = Parodi et al. (2002), SJ07 = Saviane & Jerjen (2007), C+14 = Crnojević et al. (2014), B+98 = Baggett et al. (1998), F+89 = Faber et al. (1989), D+79 = Dufour et al. (1979), GSJ12 = Gadotti & Sánchez-Janssen (2012), F+11 = Fraternali et al. (2011), W+02 = Wu et al. (2002), and W+03 = Widrow et al. (2003). Column (5): peak [Z/H] of RGB stars. Column (6): reference for [Z/H] data: H+07b = Harris et al. (2007b), LJ16 = Lee & Jang (2016), P+15 = Peacock et al. (2015), R+14 = Rejkuba et al. (2014), C+20 = this paper, M+16 = Monachesi et al. (2016), and K+06 = Kalirai et al. (2006).

circular halo (see, e.g., GSJ12), we obtain $\log(M_{10-40}/M_\odot) = 10.6$ for the Sombrero, corresponding to a total stellar halo mass of $\log(M/M_\odot) = 11.1$. Repeating these calculations for ages of 8 and 15 Gyr and a Kroupa (2001) IMF, we estimate the uncertainty of this halo mass to be of order 30% within the framework of the BaSTI models.

Using the Illustris cosmological hydrodynamical simulations, D'Souza & Bell (2018) found that the halo mass–metallicity relation found by Harmsen et al. (2017) mainly arises because the bulk of the halo mass is accreted from a single massive progenitor galaxy. From our MDF measurements described in Section 4, we derive a median metallicity of the Sombrero of [Z/H] ~ -0.07 in the radial range of 10–40 kpc. Using the scaling prescriptions of D'Souza & Bell (2018), a metallicity [Z/H] ~ -0.07, corresponding to [Fe/H] ~ -0.32 given their assumed $[\alpha/\mathrm{Fe}] = 0.3$, would imply an accreted stellar mass of $\log(M_{acc}/M_\odot) \sim 11.0 \pm 0.4$ (see Figure 5 of D'Souza & Bell 2018). Since this is equal to the total halo mass estimated above from the surface number densities of RGB stars to well within 1σ, this suggests that the accretion history of the Sombrero was dominated by a single massive merger event that occurred several gigayears ago, as opposed to our target fields being dominated by substructure due to recent, minor accretion events. In this context we note that recent wide-field ground-based imaging revealed a smooth, round halo around the Sombrero (Rich et al. 2019), which is consistent with such a major merger causing a strong gravitational perturbation that led to relatively rapid relaxation.

In terms of radial gradients of peak [Z/H] among giant ETGs and the Sombrero, the decrease of ∼0.25 dex in moving from the 16 to 33 kpc Sombrero fields turns out to be very similar to the radial gradients in giant ETGs when expressed in terms of R_{eff} (of the bulge in the case of the Sombrero; see Section 5.1.3): the radial gradients are 0.028 dex/R_{eff} for the Sombrero compared to gradients of 0.019 dex/R_{eff} (NGC 5128), 0.014 dex/R_{eff} (NGC 3115),[12] and 0.026 dex/R_{eff} (NGC 3379).

On the other hand, a more complex picture emerges when comparing the radial surface number density profiles of the metal-rich ([Z/H] > -0.8) and metal-poor ([Z/H] $\leqslant -0.8$) subpopulations. In most cases, the data show density profiles that are steeper for the metal-rich stars than for the metal-poor stars, which is consistent with the more radially extended nature of the metal-poor GC subsystems in giant ETGs (e.g.,

[12] Note, however, that this gradient for NGC 3115 should be considered a lower limit owing to incompleteness at [Z/H] $\gtrsim -0.4$ in the inner field; see Peacock et al. (2015).

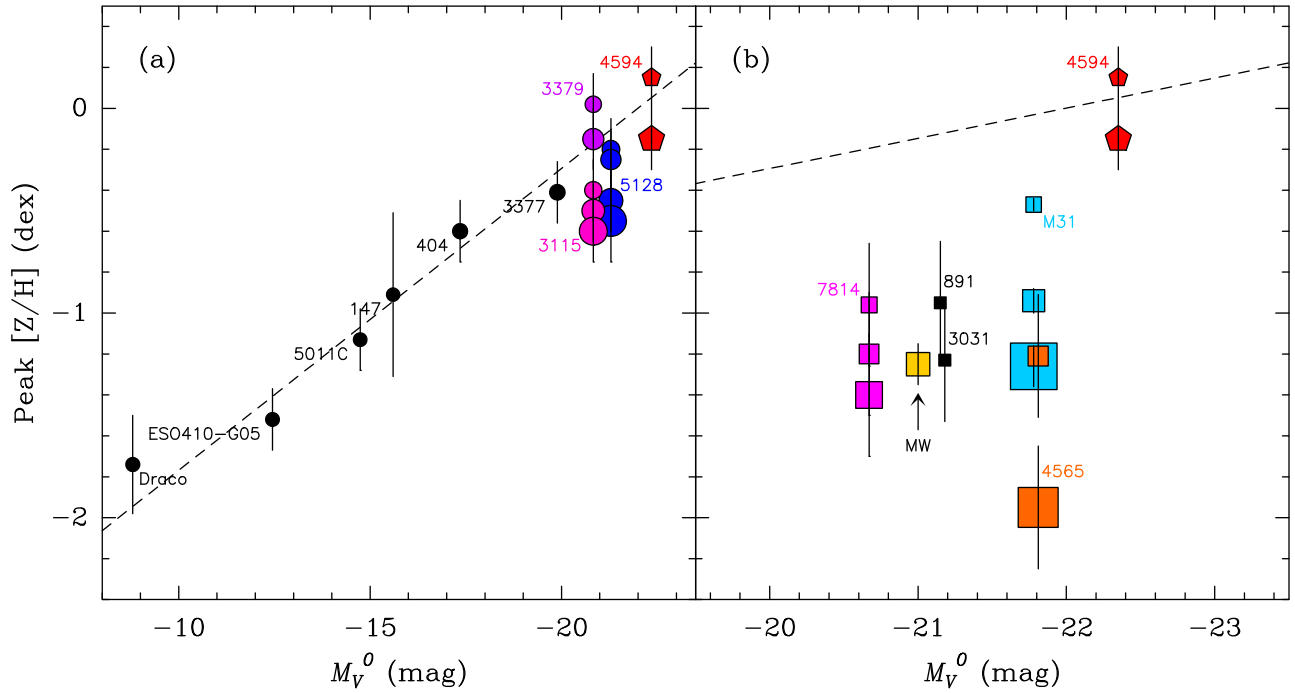

Figure 9. Peak [Z/H] of the MDF of RGB stars in halo fields around nearby galaxies as a function of galaxy M_V^0 (see Table 3). (a) Data for ETGs. Labels next to data points indicate the NGC number of the galaxy in question (unless indicated otherwise). Small black circles indicate ETG fields with $R_{gal}/R_{eff} \leqslant 5$, and the dashed line represents a linear least-squares fit to those data. Symbols and labels with colors other than black represent galaxies with more than one field, and the sizes of those symbols scale with R_{gal}/R_{eff} of the field in question. Our two halo fields in the Sombrero are represented by red pentagons. (b) Similar to panel (a), but now showing data for luminous spiral galaxies. Note the different range in M_V^0. Small black squares indicate halo fields in spirals for which the dependence of peak [Z/H] on R_{gal} is negligible according to Monachesi et al. (2016). The Milky Way halo is represented by a yellow square. The dashed line is the same one as in panel (a).

Bassino et al. 2006; Peng et al. 2008; Goudfrooij 2018). However, the differences in slope vary between host galaxies: in NGC 3379, Lee & Jang (2016) find density slopes of $\delta(\log\,\Sigma)/\delta(\log\,R_{gal}) = -3.83 \pm 0.03$ and -2.58 ± 0.03 for the metal-rich and metal-poor stars, respectively. We find a similar situation for the Sombrero, but with overall flatter density profile slopes of -2.9 ± 0.4 and -1.9 ± 0.4 for similar[13] metallicity ranges. Meanwhile, the profile slopes are very close to one another for NGC 3115 (-3.0 vs. -2.7; Peacock et al. 2015), and NGC 5128 does *not* show any significant differences in density profiles as a function of metallicity (Bird et al. 2015). This indicates that even though there are general trends among the differences in density profiles (and hence assembly histories) of metal-rich versus metal-poor subpopulations in ETG halos, there is also significant galaxy-to-galaxy scatter.

5.1.3. The Lack of RGB Stars with [Z/H] < −1

In summary, the MDF of the halo of the Sombrero shares various characteristics of other nearby massive ETGs. However, unlike any ETG studied to date, we find essentially no stars with [Z/H] < -1 in our two halo fields. Hence, if there is in fact a secondary metal-poor peak at [Z/H] < -1 as seen, for example, in NGC 3115, NGC 3379, and NGC 5128, then it must be located at even larger galactocentric radii. If we extrapolate the density profiles in Figure 8, the [Z/H] < -0.8 population would start to dominate at a projected radius of ∼70–100 kpc from the Sombrero. This would be beyond the radius where the halo is indistinguishable from the background in profiles of ground-based observations, which is $R_{gal} \sim 60$ kpc for both the integrated light (Burkhead 1986) and the GC system (Rhode & Zepf 2004).

For NGC 3379 and NGC 5128 (and, interestingly, M31 as well), the transition to a substantial metal-poor component occurs beyond $\approx 10R_{eff}$–$15R_{eff}$ (Harris et al. 2007b; Rejkuba et al. 2014). For the Sombrero, a comparison in terms of R_{eff} rather than physical radius is complicated by the question of the fundamental nature of its outer regions: the fits by GSJ12 using only a (Sérsic) bulge and (exponential) disk component find $R_{eff} = 3.3$ kpc and a bulge ellipticity of 0.42, placing our minor-axis fields at $\sim 8R_{eff}$ and $17R_{eff}$. While our nondetection of a peak at [Z/H] < -1 is already unusual in this range of R_{eff}, the three-component fit of GSJ12 that includes a power-law halo performs significantly better but yields a drastically smaller $R_{eff} \approx 0.5$ kpc (and similar bulge ellipticity of 0.46), placing even our innermost field beyond $40R_{eff}$ of the bulge, which would render the nondetection of a metal-poor component even more unusual.

5.2. Comparison to Globular Cluster Properties and Implications for Formation Scenarios

The Sombrero hosts a substantial population of GCs detected out to at least 50 kpc, with a significantly bimodal color distribution (Rhode & Zepf 2004; Dowell et al. 2014). Since the ages of the Sombrero GCs are thought to be old (Larsen et al. 2002; Hempel et al. 2007), their colors mainly reflect metallicities, allowing us to compare radial gradients in the fraction of metal-poor stars with that of metal-poor GCs. Using the extensive GC database provided by Dowell et al. (2014),

[13] The literature studies cited here typically make the division between metal-rich and metal-poor stellar populations at [Z/H] $= -0.7$. The quoted value for our density profile slope corresponds to [Z/H] > -0.6, and if we instead make this division at [Z/H] $= -0.8$, the density slope for the metal-poor population flattens to -1.2 ± 0.3.

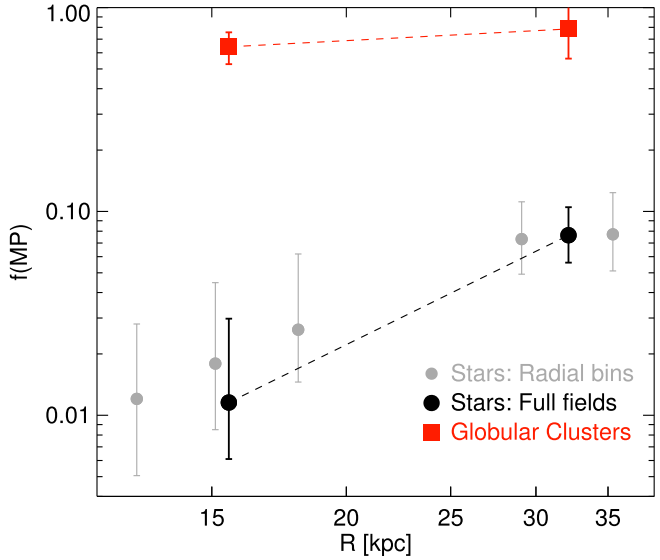

Figure 10. Fraction of metal-poor ([Z/H] < -0.8) stars as a function of galactocentric distance, shown in gray for each of the individual radial bins (identical to those used in Figures 7 and 8) and black for the UVIS and ACS fields in their entirety. For comparison, the fractions of metal-poor globular clusters at the galactocentric distances of the UVIS and ACS fields are shown as large red squares. For clarity, the full-field values are connected with dotted lines, and the y-axis is on a logarithmic scale.

we transform observed $B-R$ colors to [Z/H] according to Hargis & Rhode (2014, see their Equation (4)). Dividing the sample at [Z/H] $= -0.8$, the fraction of metal-poor GCs (hereafter $f_{\rm GC,MP}$) increases from 0.64 ± 0.11 to 0.79 ± 0.22 moving radially outward from the UVIS to ACS fields, whereas the fraction of metal-poor stars ($f_{\rm RGB,MP}$) increases from $(1.2^{+1.8}_{-0.5})\ 10^{-2}$ to $(7.6^{+2.8}_{-2.0})\ 10^{-2}$ (using the BaSTI isochrones) in the same range of $R_{\rm gal}$. These trends are illustrated in Figure 10. Such a significant offset between the fraction of metal-poor stars and metal-poor GCs in halos of ETGs was also observed in the cases of NGC 3115 (Peacock et al. 2015) and NGC 5128 (Harris & Harris 2002). However, in the Sombrero, the fraction of metal-poor stars at a given radius is lower than NGC 3115 by a factor of at least a few (modulo incompleteness at [Z/H] $\gtrsim -0.4$ in NGC 3115), and a metal-poor ([Z/H] $\lesssim -1$) peak in the stellar MDF corresponding to the blue GC subpopulation of the Sombrero (Rhode & Zepf 2004) has yet to be found.

These differences have significant implications when considering the dependence of the specific frequency of GCs ($S_N \propto N_{\rm GC}/L_V$) on metallicity in the halo of the Sombrero. In this regard we consider the ratio $S_{N,\rm MP}/S_{N,\rm MR}$, where MP and MR stand for metal-poor ([Z/H] < -0.8) and metal-rich ([Z/H] > -0.8), respectively. This ratio can be expressed as follows:

$$\frac{S_{N,\rm MP}}{S_{N,\rm MR}} = \frac{f_{\rm GC,MP}}{(1-f_{\rm GC,MP})}\,\frac{(1-f_{\rm RGB,MP})}{f_{\rm RGB,MP}}\,\frac{f_{V,\rm RGB}\ (\rm MP)}{f_{V,\rm RGB}\ (\rm MR)}, \quad (1)$$

where $f_{V,\rm RGB}(Z)$ is the fraction of SSP-equivalent V-band luminosity sampled by the observed RGB stars at metallicity Z. To determine $f_{V,\rm RGB}\,(\rm MP)$ and $f_{V,\rm RGB}\,(\rm MR)$, we assume a Chabrier (2003) IMF and use the BaSTI isochrones to determine $f_{V,\rm RGB}\,(Z)$, using the bins in [Z/H] shown in Figure 6. $f_{V,\rm RGB}\ (Z)$ is known to be strongly dependent on metallicity (see, e.g., Goudfrooij & Kruijssen 2014); we find $f_{V,\rm RGB}\,(Z) = 0.294$, 0.528, and 0.757 for [Z/H] $= 0.0$, -0.8, and -1.3, respectively. From the values of $f_{\rm GC,MP}$ and $f_{\rm RGB,MP}$ in the halo fields mentioned above, we then calculate that $S_{N,\rm MP}/S_{N,\rm MR} \approx 73$ and ≈ 23 in the Sombrero's inner and outer halo fields, respectively. While the trend of increasing S_N with decreasing metallicity is now well established among ETGs (e.g., Harris & Harris 2002; Peacock et al. 2015), the ratio $S_{N,\rm MP}/S_{N,\rm MR}$ in the Sombrero is factors of $\approx$3–10 higher than those seen in other ETG halos. Moreover, we note that the peak [Z/H] of the metal-poor GC subpopulation of the Sombrero is at [Z/H] ~ -1.5 (Hargis & Rhode 2014), a metallicity that is *completely lacking* in the RGB population of the two halo fields discussed here. This is illustrated in Figure 11, which compares the MDF of the GCs from Dowell et al. (2014) with that of the RGB stars in the two ranges in $R_{\rm gal}$. Since the metal-poor GC subsystem populates the full radial extent of the Sombrero's halo, the stellar system(s) in which the metal-poor GCs were created must currently have an S_N value that is significantly higher than any type of galaxy known in the local universe. In this regard, the highest values of S_N among nearby galaxies are found in low-mass dwarf ETGs with $-13 \lesssim M_V^0 \lesssim -11$ (Georgiev et al. 2010; see also Choksi & Gnedin 2019), with S_N values in the range of 10–70. Figure 9 suggests that such galaxies have metallicities $-1.7 \lesssim$ [Z/H] $\lesssim -1.3$, which is consistent with the blue GC subpopulation in the Sombrero and in giant ETGs (for the latter, see Peng et al. 2008; Harris et al. 2010).

An interesting possibility that can explain (at least in part) the very high S_N value at low metallicity ([Z/H] $\lesssim -1$) for the Sombrero, and for giant ETGs in general as well, is that the low-metallicity population(s) were accreted at high redshift from progenitors whose properties were different from present-day dwarf galaxies in that star formation occurred by means of an initial star cluster mass function whose low-mass truncation $M_{\rm min}$ was significantly higher than the $10^2\,M_\odot$ that is widely adopted in an environmentally independent fashion in studies of dynamical evolution of GCs (see, e.g., Lada & Lada 2003; Kruijssen 2015; Li et al. 2017). An increase of $M_{\rm min}$ implies a smaller percentage of star clusters that have dissolved completely at the present time, thus increasing S_N. Recent studies indicate that sufficiently high values of S_N result for $M_{\rm min} \gtrsim 10^3\,M_\odot$, which is expected for high-pressure starbursting environments with turbulent velocities $\sigma = 10$–$100\ {\rm km\ s^{-1}}$ and gas surface densities $\Sigma_{\rm ISM} \sim 10^2\,M_\odot\ {\rm pc^{-2}}$ (Goudfrooij 2018; Trujillo-Gomez et al. 2019), as seen in vigorously star-forming galaxies at high redshift (e.g., Tacconi et al. 2013). Future studies of lensed high-redshift galaxies with the *James Webb Space Telescope* and future 30 m class ground-based telescopes will be able to provide significantly improved constraints to S_N and the low-mass regime of the CMF in such objects and hence will allow this scenario to be tested.

5.3. Future Prospects

Our results suggest strongly that observations of halo fields in the Sombrero at even larger galactocentric radii are necessary to fully reveal the nature of its extended stellar halo. Both the increasing fraction of intermediate-metallicity stars at larger radii and the difference in metal-poor and metal-rich density profiles (Figure 8) beg for an extended radial coverage of high spatial resolution imaging that is evidently needed to

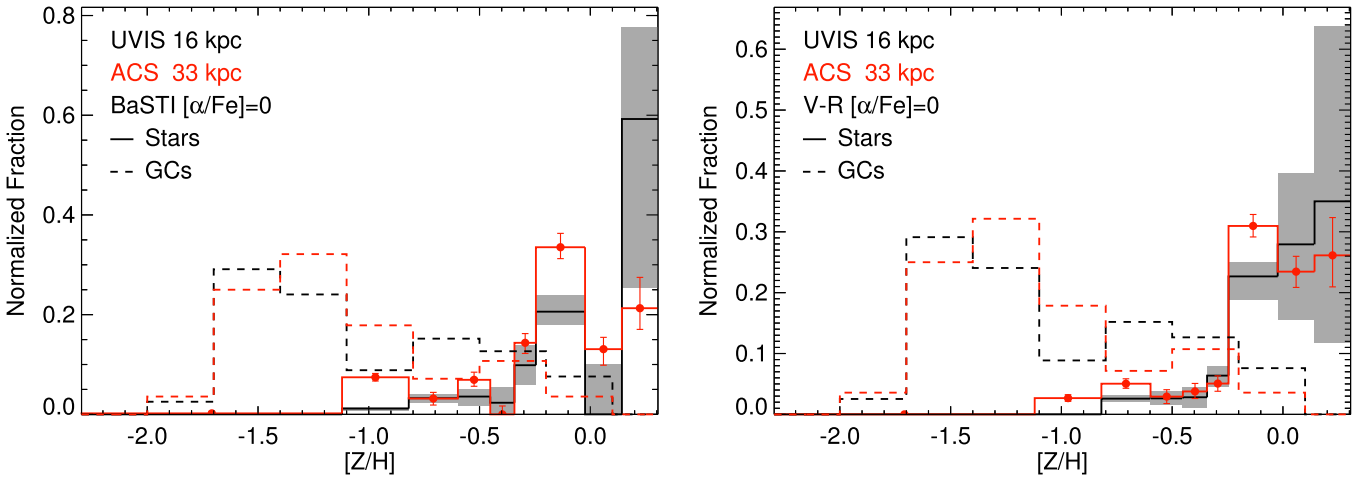

Figure 11. Stellar MDFs as in Figure 6, but now with MDFs of GCs within identical ranges of projected distance from M104 as each of our UVIS and ACS fields overplotted using dotted lines (Poissonian error bars are omitted for clarity). The fraction of metal-poor GCs is much higher than the fraction of metal-poor stars, discussed in Section 5.2.

confirm or refute the presence of a star population with $[Z/H] < -1$. Observations at larger radii, less affected by crowding, also open up two important possibilities for further constraining the formation history of the Sombrero: First, the presence or absence of substructure in MDF space, which was detected in NGC 5128 by leveraging together an ensemble of *HST* pointings probing different galactocentric radii and position angles, yields valuable clues regarding the nature and importance of past accretion events. Second, and with an eye toward forthcoming large-aperture near-infrared imaging facilities, very deep imaging to measure the red clump properties can place valuable constraints on the star formation history regarding both the age distribution (Rejkuba et al. 2005) and the metallicity distribution (e.g., Cohen et al. 2018a). Imaging at longer wavelengths would also improve our ability to characterize the MDF of the Sombrero at the high metallicities indicated by this study.

6. Summary and Conclusions

We have used deep, high-resolution *HST* imaging of two fields at 16 and 33 kpc projected galactocentric radius along the minor axis of M104 to measure MDFs in each field. Observational effects are accounted for self-consistently by forward modeling CMDs using artificial star tests and performing maximum likelihood fits to linear combinations of SSPs at varying metallicity, assuming a uniformly old (12 Gyr) population. By analyzing each field and dividing fields into bins in projected radius, we find the following results that are robust to assumptions of different evolutionary models:

1. The halo of the Sombrero galaxy is strikingly metal-rich, with its MDF peaking at near-solar metallicity, consistent with colors from optical integrated light. This is the highest peak metallicity found in halos of nearby galaxies to date. Both of our halo fields show an extreme lack of metal-poor stars: ∼90% of the stellar population has $[Z/H] \gtrsim -0.8$, even in our outermost field, which has the highest relative fraction of metal-poor stars.
2. We detect a gradient in median metallicity of $\delta[Z/H]/\delta(\log R_{gal}) \sim -0.5$ (or ~ -0.01 dex kpc^{-1}) from 16 to 33 kpc, and the fraction of metal-poor stars ($[Z/H] < -0.8$) increases by a factor of ∼6 moving radially outward but remains at $\lesssim$10% even in the outermost 33 kpc field.
3. Based on the recent analysis of the Illustris cosmological simulations by D'Souza & Bell (2018), we suggest that the metal-rich populations in the halo of the Sombrero (with a median $[Z/H] \sim -0.07$) mainly originate from a major merger with a massive galaxy with stellar mass $\log(M/M_{\odot}) \sim 11.1$, which is a substantial fraction of the current stellar mass of the Sombrero.
4. The stellar populations of the Sombrero's halo have density profiles consistent with power laws at all metallicities, although the data do not allow us to discriminate between power-law and Sérsic profiles. We find a global power-law density slope of -2.8 ± 0.4, consistent with literature surface brightness profiles. The power-law density slope exhibits a significant dependence on metallicity, with the supersolar-metallicity population falling off with a power-law slope < -3, while more metal-poor ($[Z/H] < -0.8$) stars have much flatter (> -2) density profile slopes.
5. The fraction of metal-poor GCs at the projected radii of our fields is similar to values seen for other massive early-type galaxies. While the existence of a significant offset between the fraction of metal-poor GCs and metal-poor stars is not unusual, the Sombrero is an extreme case in terms of the magnitude of this offset, with the fraction of metal-poor stars being lower than that of the metal-poor GCs by approximately an order of magnitude, and with stars with $[Z/H] < -1$ being almost completely absent, thus resulting in an extremely high specific frequency of GCs at those low metallicities. This lack of stars with $[Z/H] \lesssim -1$ at the galactocentric distances of our halo fields is unique among nearby galaxies with stellar MDF measurements in their halos. We therefore strongly suggest follow-up imaging of additional fields in the outer halo of the Sombrero to confirm or refute this apparent lack of an RGB population with $[Z/H] < -1$ in the Sombrero.

We acknowledge useful discussions with Dimitri Gadotti, and we thank the referee for a swift report with insightful suggestions that improved the paper. Support for program

HST-GO-14175 was provided by NASA through a grant from the Space Telescope Science Institute, which is operated by the Association of Universities for Research in Astronomy, Inc., under NASA contract NAS 5-26555. O.G. was supported in part by NSF through grant 1909063.

Facility: HST (ACS/WFC,WFC3/UVIS).

Appendix

Our observed CMDs and luminosity functions in Figures 2 and 3 reveal a substantial population of stars lying brightward of the Sombrero TRGB. This population is composed of a combination of photometric blends and stars scattered brightward of the TRGB by photometric errors (e.g., Harris et al. 2007a), as well as long-period RGB and AGB variables (Renzini 1998; Gregg et al. 2004). Our observations are clustered in time and are therefore not ideal for detailed variability studies. Nevertheless, to gain some insight on the influence of variables on our observed CMDs and the resulting MDFs, here we quantify variability fraction as a function of magnitude in our observed catalogs. This is done using the individual epoch observations, normalized to their uncertainties, following, e.g., Conroy et al. (2018). Specifically, for the artificial stars, which are input as nonvariable, the sum of squared deviations in the time series with respect to the mean magnitude, denoted as $F814W_{rms,norm}$, should have an average of 1, so that $\sqrt{\frac{1}{N_{obs}}\Sigma\frac{\Delta m_i}{\sigma_i}} = 1$.

First, we test the hypothesis that the *individual epoch* photometric errors reported by DOLPHOT are accurate (we know that the total reported per-filter errors are not, motivating our use of extensive artificial star tests in our MDF analysis). If this is the case, then a histogram of $F814W_{rms,norm}$ should have a peak value close to 1. We found that using the raw, reported individual epoch measurements, $F814W_{rms,norm}$ for the artificial stars is increasingly skewed to higher values at brighter magnitudes, suggesting that the individual epoch errors are somewhat underestimated, and hints of this trend are also apparent in Figure 7 of Conroy et al. (2018). We found that by increasing the individual epoch errors by ∼0.025 mag, this trend was mitigated, yielding values of $F814W_{rms,norm}$ centered on 1 for the artificial stars (note that this is an uncertainty on the *individual epoch* photometric errors and so has a negligible effect on the output *mean* magnitudes and errors. Furthermore, such an increase in individual epoch uncertainties is consistent with the margin allowed by uncertainties in aperture corrections and the absolute photometric accuracy of DOLPHOT. In any case, because candidate variables in our observed data are identified using a clip on the *distribution* of output artificial star $F814W_{rms,norm}$ versus magnitude, the sample of candidate variables is insensitive to whether we choose to apply this correction.

In Figure 12, we show for both the UVIS (left) and ACS (right) fields a histogram and cumulative distribution of $F814W_{rms,norm}$ from the artificial stars in the top panel, and in the middle panel, we define a cut versus magnitude at the 99.5% interval of the artificial star $F814W_{rms,norm}$ values calculated in sliding magnitude bins of width 0.3 mag, above which observed stars are considered to be candidate variables. In the bottom panel, we show the application of this cut to the observed time series data, and in blue we plot the variability fraction as a function of F814W magnitude. It is apparent that this variability fraction remains quite low (<10%) faintward of the TRGB, but brightward of the TRGB it increases quite rapidly.

The trend of variability fraction with magnitude supports the idea that at least half of the stars brightward of the Sombrero TRGB are variables whose light curves we are sampling stochastically, observing them with too short a time span and too limited an observing cadence to measure their mean magnitudes over their full variability cycles. This hypothesis is reinforced by variability studies of upper RGB and AGB stars in Galactic GCs, most notably for the present application including clusters with relatively high metallicities such as NGC 104 and NGC 5927. In the few cases where the necessary time baseline was achieved (e.g., Lebzelter et al. 2005; Lebzelter & Wood 2005; Arellano Ferro et al. 2015), indeed a large fraction of stars with true mean magnitudes and colors close to the TRGB are long-period or semiregular variables with both amplitudes (tenths of a magnitude or more in V) and periods (tens to hundreds of days) consistent with this idea.

The result based on Figure 12 that ∼half of the stars brighter than the TRGB are variable is a lower limit since variables with amplitudes failing our $F814W_{rms,norm}$ criterion may also be scattered above the TRGB. To test whether this is the case, we look to other contributions to the population of stars brighter than the TRGB, which come from two sources: contaminants (both foreground Milky Way stars and background galaxies) and photometric blends scattered brightward. Foreground and background contaminants account for $\lesssim$10% of the sources detected brightward of the TRGB (see Figure 5), and we can use the artificial stars to estimate the expected contribution due to blends and photometric errors. Specifically, comparing the RGB stars with magnitudes within 0.5 mag of the McQuinn et al. (2016) TRGB (shown as a red line in Figure 2) and within the same color limits of $1 \leqslant (F606W - F814W)_0 \leqslant 2.3$ (to reduce effects of incompleteness) to those with the same color limits lying brightward of the TRGB ($0.2 < F814W_{TRGB} - F814W < 1.0$), the artificial star tests predict 175 and 16 stars for the UVIS and ACS fields, respectively, in the brighter magnitude range. This ratio between the two fields is consistent with the $N_{blends} \propto \Sigma^2$ scaling predicted for photometric blends (i.e., Equation (4) of Harris et al. 2007a). Compared to the observed total numbers of stars with $0.2 < F814W_{TRGB} - F814W < 1.0$, 661 and 206 in the UVIS and ACS fields, respectively, subtracting the predicted number of blends and foreground/background contaminants predicts that the majority of sources >0.2 mag brightward of the TRGB are variables. Furthermore, the gradient in their projected densities between the UVIS and ACS fields is consistent with a power law with slope -1.9 ± 0.3, in good agreement with the stellar projected density gradients shown in Figure 8, especially given that our color cut is biased toward the relatively more metal-poor component.

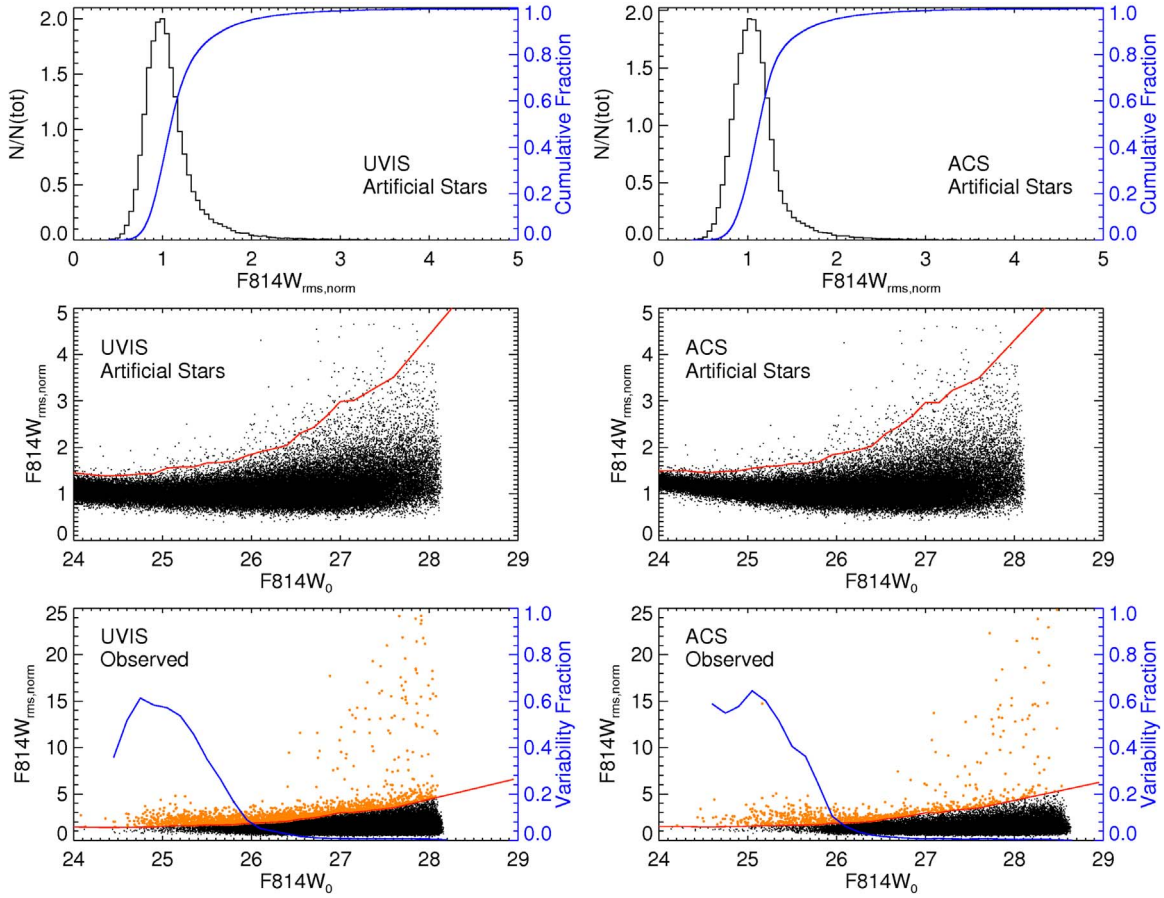

Figure 12. For the UVIS (left) and ACS (right) fields. Top: histogram of $F814W_{rms,norm}$ for input artificial stars that are assumed to be constant. The cumulative distribution of $F814W_{rms,norm}$ is overplotted in blue with respect to the right-hand axis. Values shown here are after adding an additional per-epoch uncertainty of 0.025 mag (see text). Middle: trend of $F814W_{rms,norm}$ with F814W magnitude for the artificial stars. Our criterion for defining variables from the 99.5% observed envelope is overplotted in red. Bottom: $F814W_{rms,norm}$ vs. mean F814W for observed stars, with our variability criterion overplotted and candidate variables shown in orange (note the difference in *y*-axis scale compared with the middle panel). The variability fraction is overplotted in blue with respect to the right-hand axis.

ORCID iDs

Paul Goudfrooij https://orcid.org/0000-0002-5728-1427
Matteo Correnti https://orcid.org/0000-0001-6464-3257
Oleg Y. Gnedin https://orcid.org/0000-0001-9852-9954
William E. Harris https://orcid.org/0000-0001-8762-5772
Rupali Chandar https://orcid.org/0000-0003-0085-4623
Thomas H. Puzia https://orcid.org/0000-0003-0350-7061

References

Arellano Ferro, A., Bramich, D. M., Giridhar, S., Luna, A., & Muneer, S. 2015, IBVS, 6137, 1
Baggett, W. E., Baggett, S. E., & Anderson, K. S. J. 1998, AJ, 116, 1626
Bassino, L. P., Cellone, S. A., Forte, J. C., & Dirsch, B. 2006, A&A, 451, 789
Bernard, E. J., Schultheis, M., Di Matteo, P., et al. 2018, MNRAS, 477, 3507
Bird, S. A., Flynn, C., Harris, W. E., & Valtonen, M. 2015, A&A, 575, A72
Bohlin, R. C. 2012, ACS Instrument Science Rep. 2012-01 (Baltimore: STScI)
Brown, T. M., Smith, E., Ferguson, H. C., et al. 2009, ApJS, 184, 152
Bruzual, G., & Charlot, S. 2003, MNRAS, 344, 1000
Burkhead, M. S. 1986, AJ, 91, 777
Casagrande, L., & VandenBerg, D. A. 2014, MNRAS, 444, 392
Chabrier, G. 2003, PASP, 115, 763
Choksi, N., & Gnedin, O. Y. 2019, MNRAS, 488, 5409
Cohen, R. E., Kalirai, J. S., Gilbert, K. M., et al. 2018a, AJ, 156, 230
Cohen, R. E., Mauro, F., Alonso-García, J., et al. 2018b, AJ, 156, 41
Conroy, C., Strader, J., van Dokkum, P., et al. 2018, ApJ, 864, 111
Cooper, A. P. 2017, in Proc. IAU Symp. 321, Formation and Evolution of Galaxy Outskirts, ed. A. G. de Paz, J. C. Lee, & J. H. Knapen (Cambridge: Cambridge Univ. Press), 69
Cooper, A. P., Parry, O. H., Lowing, B., Cole, S., & Frenk, C. 2015, MNRAS, 454, 3185
Crnojević, D., Ferguson, A. M. N., Irwin, M. J., et al. 2013, MNRAS, 432, 832
Crnojević, D., Ferguson, A. M. N., Irwin, M. J., et al. 2014, MNRAS, 445, 3862
Deustua, S. E., Mack, J., Bajaj, V., & Khandrika, H. 2017, WFC3 Instrument Science Rep. 2017-14 (Baltimore: STScI)
Deustua, S. E., Mack, J., Bowers, A. S., et al. 2016, WFC3 Instrument Science Rep. 2016-03
de Vaucouleurs, G., de Vaucouleurs, A., Corwin, H. G., Jr., et al. 1991, Third Reference Catalogue of Bright Galaxies (New York: Springer)
Dolphin, A. E. 2000, PASP, 112, 1383
Dolphin, A. E. 2002, MNRAS, 332, 91
Dong, H., Schödel, R., Williams, B. F., et al. 2017, MNRAS, 470, 3427
Dowell, J. L., Rhode, K. L., Bridges, T. J., et al. 2014, AJ, 147, 150
D'Souza, R., & Bell, E. F. 2018, MNRAS, 474, 5300
Dufour, R. J., Harvel, C. A., Martins, D. M., et al. 1979, AJ, 84, 284
Durrell, P. R., Sarajedini, A., & Chandar, R. 2010, ApJ, 718, 1118
Emsellem, E., Bacon, R., Monnet, G., & Poulain, P. 1996, A&A, 312, 777
Faber, S. M., Wegner, G., Burstein, D., et al. 1989, ApJS, 69, 763
Fraternali, F., Sancisi, R., & Kamphuis, P. 2011, A&A, 531, A64
Gadotti, D. A., & Sánchez-Janssen, R. 2012, MNRAS, 423, 877, (GSJ12)
Gallazzi, A., Charlot, S., Brinchmann, J., White, S. D. M., & Tremonti, C. A. 2005, MNRAS, 362, 41
Georgiev, I. Y., Puzia, T. H., Goudfrooij, P., & Hilker, M. 2010, MNRAS, 406, 1967
Girardi, L., Barbieri, M., Groenewegen, M. A. T., et al. 2012, Red Giants as Probes of the Structure and Evolution of the Milky Way (Berlin: Springer), 165
Girardi, L., Groenewegen, M. A. T., Hatziminaoglou, E., & da Costa, L. 2005, A&A, 436, 895

Goddard, D., Thomas, D., Maraston, C., et al. 2017, MNRAS, 466, 4731
Gonzaga, S., Hack, W., Fruchter, A. S., & Mack, J. (ed.) 2012, The DrizzlePac Handbook (Baltimore: STScI)
Goudfrooij, P. 2012, ApJ, 750, 140
Goudfrooij, P. 2018, ApJ, 857, 16
Goudfrooij, P., & Kruijssen, J. M. D. 2014, ApJ, 780, 43
Goudfrooij, P., Strader, J., Brenneman, L., et al. 2003, MNRAS, 343, 665
Greene, J. E., Murphy, J. D., Graves, G. J., et al. 2013, ApJ, 776, 64
Greene, J. E., Veale, M., Ma, C.-P., et al. 2019, ApJ, 874, 66
Gregg, M. D., Ferguson, H. C., Minniti, D., Tanvir, N., & Catchpole, R. 2004, AJ, 127, 1441
Guérou, A., Emsellem, E., Krajnović, D., et al. 2016, A&A, 591, A143
Hargis, J. R., & Rhode, K. L. 2014, ApJ, 796, 62
Harmsen, B., Monachesi, A., Bell, E. F., et al. 2017, MNRAS, 466, 1491
Harris, J., & Zaritsky, D. 2001, ApJS, 136, 25
Harris, J., & Zaritsky, D. 2012, StarFISH: For Inferring Star-formation Histories, Astrophysics Source Code Library, ascl:1204.008
Harris, W. E. 1996, AJ, 112, 1487
Harris, W. E., & Harris, G. L. H. 2002, AJ, 123, 3108
Harris, W. E., Harris, G. L. H., Layden, A. C., & Stetson, P. B. 2007a, AJ, 134, 43
Harris, W. E., Harris, G. L. H., Layden, A. C., & Wehner, E. M. H. 2007b, ApJ, 666, 903
Harris, W. E., Spitler, L. R., Forbes, D. A., & Bailin, J. 2010, MNRAS, 401, 1965
Hempel, M., Zepf, S., Kundu, A., Geisler, D., & Maccarone, T. J. 2007, ApJ, 661, 768
Hidalgo, S. L., Aparicio, A., Skillman, E., et al. 2011, ApJ, 730, 14
Jang, I. S., & Lee, M. G. 2015, ApJ, 807, 133
Jardel, J. R., Gebhardt, K., Shen, J., et al. 2011, ApJ, 739, 21
Kalirai, J. S., Gilbert, K. M., Guhathakurta, P., et al. 2006, ApJ, 648, 389
Kirby, E. N., Cohen, J. G., Guhathakurta, P., Cheng, L., Bullock, J. S., & Gallazzi, A. 2013, ApJ, 779, 102
Kormendy, J., & Kennicutt, R. C., Jr. 2004, ARA&A, 42, 603
Kroupa, P. 2001, MNRAS, 322, 231
Kruijssen, J. M. D. 2015, MNRAS, 454, 1658
Lada, C. J., & Lada, E. A. 2003, ARA&A, 41, 57
Larsen, S. S., Brodie, J. P., Beasley, M. A., & Forbes, D. A. 2002, AJ, 124, 828
Lebzelter, T., & Wood, P. R. 2005, A&A, 441, 1117
Lebzelter, T., Wood, P. R., Hinkle, K. H., Joyce, R. R., & Fekel, F. C. 2005, A&A, 432, 207
Lee, M. G., & Jang, I. S. 2016, ApJ, 822, 70
Li, H., Gnedin, O. Y., Gnedin, N. Y., et al. 2017, ApJ, 834, 69
Li, H., Mao, S., Cappellari, M., et al. 2018, MNRAS, 476, 1765
Li, Z., Wang, Q. D., & Hameed, S. 2007, MNRAS, 376, 960
Lotz, J. M., Koekemoer, A., Coe, D., et al. 2017, ApJ, 837, 97
Mackereth, J. T., Schiavon, R. P., Pfeffer, J., et al. 2019, MNRAS, 482, 3426
Maybhate, A., Goudfrooij, P., Chandar, R., & Puzia, T. H. 2010, ApJ, 721, 893
McConnachie, A. W. 2012, AJ, 144, 4
McDermid, R. M., Alatalo, K., Blitz, L., et al. 2015, MNRAS, 448, 3484
McQuinn, K. B. W., Skillman, E. D., Dolphin, A. E., Berg, D., & Kennicutt, R. 2016, AJ, 152, 144
Mihos, J. C., Durrell, P. R., Feldmeier, J. J., Harding, P., & Watkins, A. E. 2018, ApJ, 862, 99
Monachesi, A., Bell, E. F., Radburn-Smith, D. J., et al. 2016, MNRAS, 457, 1419
Monachesi, A., Gómez, F. A., Grand, R. J. J., et al. 2019, MNRAS, 485, 2589
Moretti, A., Held, E. V., Rizzi, L., et al. 2003, in Extragalactic Globular Cluster Systems, ed. M. Kissler-Patig (Berlin: Springer), 167
Mouhcine, M., Ferguson, H. C., Rich, R. M., Brown, T. M., & Smith, T. E. 2005a, ApJ, 633, 821
Mouhcine, M., Rich, R. M., Ferguson, H. C., Brown, T. M., & Smith, T. E. 2005b, ApJ, 633, 828
Mould, J., & Spitler, L. 2010, ApJ, 722, 721
Nataf, D. M., Gould, A. P., Pinsonneault, M. H., & Udalski, A. 2013, ApJ, 766, 77
Oser, L., Ostriker, J. P., Naab, T., Johansson, P. H., & Burkert, A. 2010, ApJ, 725, 2312
Parodi, B. R., Barazza, F. D., & Binggeli, B. 2002, A&A, 388, 29
Pastorello, N., Forbes, D. A., Foster, C., et al. 2014, MNRAS, 442, 1003
Peacock, M. B., Strader, J., Romanowsky, A. J., & Brodie, J. P. 2015, ApJ, 800, 13
Peng, E. W., Jordán, A., Côté, P., et al. 2008, ApJ, 639, 95
Pietrinferni, A., Cassisi, S., Salaris, M., & Castelli, F. 2004, ApJ, 612, 168
Pietrinferni, A., Cassisi, S., Salaris, M., & Castelli, F. 2006, ApJ, 642, 797
Portegies Zwart, S. F., McMillan, S. L. W., & Gieles, M. 2010, ARA&A, 48, 431
Puzia, T. H., Paolillo, M., Goudfrooij, P., et al. 2014, ApJ, 786, 78
Radburn-Smith, D. J., de Jong, R. S., Seth, A. C., et al. 2011, ApJS, 195, 18
Rejkuba, M., Greggio, L., Harris, W. E., Harris, G. L. H., & Peng, E. W. 2005, ApJ, 631, 262
Rejkuba, M., Harris, W. E., Greggio, L., et al. 2014, ApJL, 791, L2
Renzini, A. 1998, AJ, 115, 2459
Rhode, K. L., & Zepf, S. E. 2004, AJ, 127, 302
Rich, R. M., Mosenkov, A., Lee-Saunders, H., et al. 2019, MNRAS, 490, 1539
Rizzi, L., Tully, R. B., Makarov, D., et al. 2007, ApJ, 661, 815
Ryan, S. G., & Norris, J. E. 1991, AJ, 101, 1865
Saviane, I., & Jerjen, H. 2007, AJ, 133, 1756
Schlafly, E. F., & Finkbeiner, D. P. 2011, ApJ, 737, 103
Schlegel, D. J., Finkbeiner, D. P., & Davis, M. 1998, ApJ, 500, 525
Spitler, L. R., Larsen, S. S., Strader, J., et al. 2006, AJ, 132, 1593
Tacconi, L. J., Neri, R., Genzel, R., et al. 2013, ApJ, 768, 74
Tempel, E., & Tenjes, P. 2006, MNRAS, 371, 1269
Trujillo-Gomez, S., Reina-Campos, M., & Kruijssen, J. M. D. 2019, MNRAS, 488, 3972
VandenBerg, D. A., Bergbusch, P. A., Ferguson, J. W., & Edvardsson, B. 2014, ApJ, 794, 72
VandenBerg, D. A., Swenson, F. J., Iglesias, C. A., & Alexander, D. R. 2000, ApJ, 532, 430
Webb, J. J., Sills, A., & Harris, W. E. 2013, ApJ, 779, 94
Widrow, L. M., Perrett, K. M., & Suyu, S. H. 2003, ApJ, 588, 311
Williams, B. F., Lang, D., Dalcanton, J. J., et al. 2014, ApJS, 215, 9
Woodley, K. A., & Gómez, M. 2010, PASA, 27, 379
Wu, H., Burstein, D., Deng, Z., et al. 2002, AJ, 123, 1364
Young, L. M., Scott, N., Serra, P., et al. 2014, MNRAS, 444, 3408